

Pulsational Pair-instability Supernovae. I. Pre-collapse Evolution and Pulsational Mass Ejection

SHING-CHI LEUNG,^{1,2} KEN'ICHI NOMOTO,¹ AND SERGEI BLINNIKOV^{1,3,4}

¹*Kavli Institute for the Physics and Mathematics of the Universe (WPI), The University of Tokyo Institutes for Advanced Study, The University of Tokyo, Kashiwa, Chiba 277-8583, Japan*

²*TAPIR, Walter Burke Institute for Theoretical Physics, Mailcode 350-17, Caltech, Pasadena, CA 91125, USA*

³*NRC "Kurchatov Institute" – ITEP, B. Cheremushkinkaya 25, 117218 Moscow, Russia*

⁴*Dukhov Automatics Research Institute (VNIIA), Sushevskaya 22, 127055 Moscow, Russia*

(Dated: January 1, 2020)

ABSTRACT

We calculate the evolution of massive stars, which undergo pulsational pair-instability (PPI) when the O-rich core is formed. The evolution from the main-sequence through the onset of PPI is calculated for stars with the initial masses of 80 – 140 M_{\odot} and metallicities of $Z = 10^{-3} - 1.0 Z_{\odot}$. Because of mass loss, $Z \leq 0.5 Z_{\odot}$ is necessary for stars to form He cores massive enough (i.e., mass $> 40 M_{\odot}$) to undergo PPI. The hydrodynamical phase of evolution from PPI through the beginning of Fe core collapse is calculated for the He cores with masses of 40 – 62 M_{\odot} and $Z = 0$. During PPI, electron-positron pair production causes a rapid contraction of the O-rich core which triggers explosive O-burning and a pulsation of the core. We study the mass dependence of the pulsation dynamics, thermodynamics, and nucleosynthesis. The pulsations are stronger for more massive He cores and result in such a large amount of mass ejection such as 3 – 13 M_{\odot} for 40 – 62 M_{\odot} He cores. These He cores eventually undergo Fe-core collapse. The 64 M_{\odot} He core undergoes complete disruption and becomes a pair-instability supernova. The H-free circumstellar matter ejected around these He cores is massive enough for to explain the observed light curve of Type I (H-free) superluminous supernovae with circumstellar interaction. We also note that the mass ejection sets the maximum mass of black holes (BHs) to be $\sim 50 M_{\odot}$, which is consistent with the masses of BHs recently detected by VIRGO and aLIGO.

Keywords: stars: oscillations (including pulsations) – (stars:) supernovae: general – stars: evolution – (stars:) circumstellar matter – stars: black holes

1. INTRODUCTION

1.1. Pulsational Pair-Instability (PPI)

The structure and evolution of massive stars depend on stellar mass, metallicity, and rotation (e.g., Arnett 1996; Nomoto & Hashimoto 1988; Heger et al. 2000; Heger & Woosley 2002; Nomoto et al. 2013; Meynet & Maeder 2017; Limongi 2017; Hirschi 2017). In stars with the zero-age main-sequence (ZAMS) mass of $M \sim 10 - 80 M_{\odot}$, hydrostatic burning progresses from light elements to heavy elements in the sequence of H, He, C, O, Ne, and Si burning, and finally a Fe core forms and gravitationally collapses to form a compact object such as a neutron star.

For very massive stars with $M \gtrsim 80 M_{\odot}$ (i.e. a He core of mass greater than 35 M_{\odot}), but exact correspondence is strongly metallicity dependent (El Eid et al. 1983; Heger & Woosley 2002; Hirschi 2017; Woosley

2017), effects of the electron-positron pair-production ($\gamma \rightarrow e^{-} + e^{+}$) on stellar structure and evolution are important when the O-rich core is formed (Fowler & Hoyle 1964; Fraley 1968). Pair-production causes the dynamically unstable contraction of the O-rich core, which ignites explosive O-burning. For $140 M_{\odot} \lesssim M \lesssim 300 M_{\odot}$, the released nuclear energy is large enough to disrupt the whole star, so that the star explodes as pair-instability supernovae (PISN) (Barkat et al. 1967; Bond et al. 1984; Baraffe et al. 2001). Above $\sim 300 M_{\odot}$, the star collapses to form black hole again. As a result, no black hole can be formed with a mass between $\sim 50 M_{\odot}$ and $\sim 150 M_{\odot}$ (Heger & Woosley 2002). Such mass gap may provide distinctive features in the mass spectrum of black hole through the detection of merger event of binary black holes.

For stars with $M = 80 - 140 M_{\odot}$ [He cores of $35 - \sim 65 M_{\odot}$ (Woosley 2017)], explosive O burning does not disrupt the whole star, but creates strong pulsations (Barkat et al. 1967; Rakavy & Shaviv 1967), which is called Pulsational Pair-instability (PPI). These stars undergo distinctive evolution compared to more massive or less massive stars. PPI is strong enough to induce massive mass ejection as in PISN, while the star further evolves to form an Fe core that collapses into a compact object later as a core collapse supernova (CCSN). PPI supernovae (PPISNe) of $80 - 140 M_{\odot}$ stars are thus the hybrid of PISN and CCSN.

The exact ZAMS mass range of PPISN depends on the mass loss by stellar wind, thus on metallicity, and also on rotation. For PPISN progenitors, the wind mass loss during H and He burning phases could contribute to the loss of almost a half of the initial progenitor mass (See e.g. Table 2 of Woosley (2017)). Such mass loss can suppress the formation of a massive He-core. The exact mass of the He core as a function of metallicity and ZAMS mass remains less understood because the mass loss processes in massive star are not well constrained (Renzo et al. 2017). Rotation provides additional support by the centripetal force, which allows PPISN to be formed at an even higher progenitor mass (Glatzel et al. 1985; Chatzopoulos & Wheeler 2012).

In order to pin down the mass range of PPISN, a mass survey of main-sequence star models is done in Heger & Woosley (2002); Ohkubo et al. (2009) with focus on the zero metallicity stars. Large surveys in other metallicity can be also found in e.g. Heger & Woosley (2010); Sukhbold et al. (2016). A large array of stellar models covering also PPISN with rotation has been further explored in Yoon et al. (2012).

The evolution of PPISN is very dynamical in the late phase. During the pulsation, the dynamical timescale can be comparable with the nuclear timescale that hydrostatic approximation is no longer a good approximation. Also, when the star drastically expands after the energetic nuclear burning triggered at the contraction, the subsequent shock breakout near the surface is obviously a dynamical phenomenon. This suggests that during this dynamical but short phase, hydrodynamics instead of hydrostatic is required in order to follow the evolution consistently. Compared to hydrodynamical studies of PISNe (Barkat et al. 1967; Umeda & Nomoto 2002; Heger & Woosley 2002; Scammapieco et al. 2005; Chatzopoulos et al. 2013; Chen et al. 2014), systematic hydrodynamical study of PPI has been conducted only recently (e.g., Woosley & Heger 2015; Woosley 2017).

1.2. Connections to Observations

The optical aspect of PPI and PPISN might explain some super-luminous supernovae (SLSNe), such as SN2006gy (Woosley et al. 2007; Kasen et al. 2011; Chen et al. 2014). Recent modelling of SLSN PTF12dam (Tolstov et al. 2017) has required an explosion of a $40 M_{\odot}$ star with $20 - 40 M_{\odot}$ circumstellar medium (CSM) with a sum of $6 M_{\odot}$ ^{56}Ni in the explosion. The shape, rising time and fall rate of the light curves provide constraints on the composition, density and velocity of the ejecta, which give insights to the modeling of PPISN. It demonstrates the importance to track the mass loss history of a star prior to its collapse. The rich mass ejection can be an explanation to the dense CSM observed in some supernovae, such as SN 2006jc (Foley et al. 2007). Supernova models in the PPISN mass range are further applied to explain some unusual objects, including SN 2007bi (Moriya et al. 2010; Yoshida et al. 2014) and iPTF14hls (Woosley 2018).

There is also a possible connection to the well observed Eta Carinae, which has demonstrated significant mass loss of about $30 M_{\odot}$ (Smith et al. 2007; Smith 2008).

Furthermore, recent detections of the gravitational waves emitted by the merging of black holes (BH) (Abbott et al. 2016a,b), such as GW150914 and GW170729 imply existence of BHs of masses $\sim 30 - 50 M_{\odot}$. In order to study the mass spectrum of BHs in this mass range, the evolutionary path of this class of objects becomes necessary. Such observations have led to the interest in the evolutionary origin of massive BHs, including PPI phenomena (e.g., Woosley 2017; Belczynski et al. 2017; Marchant et al. 2018). Our calculations will update the lower end of the "mass gap" of the massive BHs (not near the NS-BH boundary).

1.3. Present Study

From the above importance of PPI, we re-examine PPI by using the open-source stellar evolution code MESA (v8118; Paxton et al. (2011, 2013, 2015, 2017)).

We use this version because the recent update of the code (Paxton et al. 2015) has included an implicit energy-conserving (Grott et al. 2005) hydrodynamical scheme as one of its evolution options.

We study a series of the evolution of stars from ZAMS for the masses ranging from 80 to $140 M_{\odot}$ and various metallicities. This corresponds to the He-core masses from ~ 40 to $65 M_{\odot}$. Then we calculate the evolution of such He stars to study the hydrodynamical behaviour of PPI including mass ejection.

In Section 2 we describe the code for preparing the initial models and the details of the one-dimensional implicit hydrodynamics code for the pulsation phase.

In Section 3 we examine the evolutionary path of PPISN in the H and He-burning phases and the influence of metallicity on the final He and CO-core masses.

Then in Section 4, we first present the pre-pulsation evolution of our models which includes He- and C-burning phases. We study the dynamics of the pulsation and its effects on the shock-induced mass loss. After that, we present evolution models of He cores with 40 - 64 M_{\odot} . We examine their properties from four aspects, the thermodynamic, mass loss, energetics and chemical properties.

In Section 5 we examine the connections of our models to super-luminous supernova progenitors.

In Section 6 we compare the final stellar mass of our PPISN models with the recently measured black hole masses detected by gravitational wave signals.

In Section 7 we conclude our results.

We present in the Appendix A our numerical models with those in the literature. In Appendix B and Appendix C the effects of some physical inputs in the numerical modeling, including the convective mixing and artificial viscosity.

2. METHODS

2.1. *Stellar Evolution*

To prepare the pre-collapse model, we use the open source code Modules for Experiments in Stellar Astrophysics (MESA) (v8118; Paxton et al. (2011, 2013, 2015, 2017)). It is a one-dimensional stellar evolution code. Recent updates of this code have also included packages for stellar pulsation analysis and implicit hydrodynamics extension with artificial viscosity. We modify the package *ccsn* to build a He-core or main-sequence star models directly and then we switch to the hydrodynamics formalism according to the global dynamical timescale of the star.

2.2. *Hydrodynamics*

To understand the behaviour of pulsation and runaway burning in the O-core, we use the one-dimensional implicit hydrodynamics option. This option appears in the third instrument paper (Paxton et al. 2015). The energy conserving scheme, coupled with the implicit mass-conserving property of the Lagrangian formalism, allows us to trace the evolution of the star consistently.

We refer the readers to the instrument paper Paxton et al. (2015) (Section 4) where the detailed implementation of this mass- and energy-conserving implicit hydrodynamics scheme is documented. Here we briefly outline the specific points which are relevant to our calculation here.

The realization of this scheme relies on the use of artificial viscosity as a substitute to the exact Riemann solver. To capture the shock, the artificial viscosity takes the form

$$Q_i = -C_a \rho_i \frac{4\pi r_i^6}{dm_i} \left(\frac{v_{i+1}}{r_{i+1}} - \frac{v_i}{r_i} \right), \quad (1)$$

which has the same unit as the pressure term and it enters the system of equations by $P \rightarrow (P + Q)$. v_i and r_i are the velocity and radius of the mass shell i defined at the cell boundary. dm_i is the mass of the fluid element. We choose $C_a = 0.002 - 0.02$. However, the value of C_a is needed to be chosen by experience. A too large C_a may dissipate too early the propagation of outgoing waves, which artificially suppresses the mass loss. A too small C_a may create numerical difficulties when the shock becomes too strong for the hydrodynamics to handle, especially near the surface. We study the effects on the choice of C_a in the Appendix C.

We define the physical quantities of convention as follows. Density, temperature, isotope mass fractions, specific internal and related thermodynamics quantities are defined at the cell centers. Position, velocity, acceleration and gravity source terms are defined at the cell boundaries. We impose the innermost boundary conditions as $r_0 = 0$.

The typical timescale during the pulsation is comparable to the dynamical timescale. However, after the pulsation phase, it is the Kelvin-Helmholtz (KH) timescale that dominates the contraction. Even with the implicit nature of the dynamics code, simply using the hydrodynamics formalism to evolve the whole pulsation phase is computationally challenging as the Courant-Friedrich-Levy condition limits the maximum possible timescale, despite the virtue of consistency in our calculation. We set conditions for the code to switch back to the hydrostatic approximation. When the star sufficiently expands after bounce so that the evolutionary timescale is dominated by thermal timescale, we increase the maximum timestep at every 100 steps. When the star can evolve continuously with the maximum timestep (10^5 times of Courant timestep), we change to the hydrostatic approximation to evolve the star until another pulsation starts. If the star appears to be non-static during the 100-step buffer, the buffer is extended until the star is fully relaxed. The convective mixing is also switched on only in the hydrostatic mode. In general, we find that dynamical treatment is necessary when the central temperature of the star exceeds $10^{9.3}$ K.

In the pulsation phase, once the expansion of the star reaches the surface, it develops into a high velocity outburst due to the density gradient near the surface. The fluid elements can have a velocity larger than the escape

velocity. The ejected mass is dynamically irrelevant to the core evolution. We remove from those mass elements which satisfy this condition and have a density below $10^{-6} \text{ g cm}^{-3}$. We set a mass loss rate according to how fast the outermost shell leaves our system according to its velocity. To avoid removing mass shell in an unphysical rate due to interpolation, the mass loss rate is capped above.

2.3. Microphysics

The code uses the Helmholtz equation of state (Timmes & Arnett 1999), which contains electron gas with arbitrary relativistic and degeneracy levels, ions in the form of a classical ideal gas, photon gas with Planck distribution and electron-positron pairs. To model the nuclear reactions, we use the *'approx21_plus_co56.net'* network. This includes the α -chain network (^4He , ^{12}C , ^{16}O , ^{20}Ne , ^{24}Mg , ^{28}Si , ^{32}S , ^{36}Ar , ^{40}Ca , ^{44}Ti , ^{48}Cr , ^{52}Fe and ^{56}Ni), ^1H , ^3He and ^{14}N for the hydrogen burning and CNO cycle, and ^{56}Fe and ^{56}Co to trace the decay chain of ^{56}Ni . ^{56}Cr is included to mimic the neutron-rich isotopes formed after electron capture in nuclear statistical equilibrium (NSE).

The MESA EOS is a blend of the OPAL (Rogers & Nayfonov 2002), SCVH (Saumon et al. 1995), PTEH (Pols et al. 1995), HELM (Timmes & Swesty 2000), and PC (Potekhin & Chabrier 2010) EOSes.

Radiative opacities are primarily from OPAL (Iglesias & Rogers 1993, 1996), with low-temperature data from (Ferguson et al. 2005) and the high-temperature, Compton-scattering dominated regime by (Buchler & Yueh 1976). Electron conduction opacities are from (Cassisi et al. 2007).

Nuclear reaction rates are from JINA REACLIB (Cyburt et al. 2010) plus additional tabulated weak reaction rates (Fuller et al. 1985; Oda et al. 1994; Langanke & Martínez-Pinedo 2000). Screening is included via the prescription of (Salpeter 1954; Dewitt et al. 1973; Alastuey & Jancovici 1978; Itoh et al. 1979). Thermal neutrino loss rates are from Itoh et al. (1996).

2.4. Convective Mixing

As indicated in Woosley (2017), convective mixing is important that it redistributes the fuel and ash in the remnant core. This affects the subsequent nuclear burning when the star contracts again. We choose the Mixing Length Theory (MLT) (Böhm-Vitense 1958) (See e.g. Cox & Giuli (1968) for a realization) to model the convective process with Schwarzschild criterion. The MLT approximation is used in the main-sequence phase and also when the star enters the expansion phase.

We have attempted to couple the convective mixing in the dynamical phase but it results in numerical instabilities. We notice that the convective timescale during

the dynamical phase is longer than dynamical timescale. Furthermore, the more massive the star is, the burning timescale and its contraction timescale due to PPI decrease. The mixing process becomes more inefficient compared to the lower mass stars. Since we are interested to the mass loss process of PPISN, this means to a good approximation by neglecting convection. (Also see Section 4 the corresponding Kippenhahn Diagrams). Therefore, it becomes numerically manageable while physically consistent to ignore convective mixing in the dynamical phase.

However, we also notice that in the lower mass regime (e.g. $40 M_{\odot}$ case), the contraction timescale is on the contrary long that the convective mixing becomes more important. In the Appendix we examine the importance of mixing to the pulsation history for the lower mass PPISN. We remind that during pulsations not only convective mixing is suppressed, but also convective energy transport is suppressed. This plays a major role in the weak pulsations found by other authors, as the ones shown in the Models He36 and He40 in Figure 3 of Woosley (2017). In these cases there is only a mild collapse, and the energy produced through nuclear burning can be transported by convection without an eruption.

3. EVOLUTION OF PPISN PROGENITORS

In this section we cover the methodology and the results for the stellar evolution model based on H main-sequence stars and run until the central temperature reaches $10^{9.4} \text{ K}^1$. We choose the *Dutch* mass loss rate (an ensemble of mass loss rates computed separately in Vink et al. (2001); Glebbeek et al. (2009)) for hot hydrogen rich stars, Nugis & Lamers (2000) for hot hydrogen poor stars, and de Jager et al. (1988) for winds from cold stars. The scaling factor follows Maeder & Meynet (2001) for modeling non-rotating stars.

3.1. Evolution in Kippenhahn Diagram

In Figures 1, 2 and 3, we plot the Kippenhahn Diagram of the stars with $M = 80, 100$ and $120 M_{\odot}$ at $Z = Z_{\odot}$. The lines (red, green and blue) correspond to the He-, C- and O- core mass coordinate respectively. Grey shaded regions are the convective zones inside the star. All models are run until the core reaches a central temperature of $10^{9.4} \text{ K}$.

At solar metallicity the high metal content in the initial composition has largely increased the opacity, which allows strong mass loss during H-burning and He-burning due to its intrinsic high luminosity. It has an

¹ We uploaded the related configuration files used in our simulations in DOI:10.5281/zenodo.3457295

Table 1. The pre-pulsation He core mass at the exhaustion of H in the core. The numbers in brackets are the CO core mass at the exhaustion of He in the core. All masses are in units of solar mass.

¹ The models assume no mass loss.

Mass (M_{\odot})	$Z = 10^{-3} Z_{\odot}$ ¹	$Z = 10^{-2} Z_{\odot}$ ¹	$Z = 0.1 Z_{\odot}$	$Z = 0.5 Z_{\odot}$	$Z = 0.75 Z_{\odot}$	$Z = 1 Z_{\odot}$
80	34.05	37.40 (27.20)	33.80 (23.93)	30.10 (23.96)	23.60 (21.09)	22.70 (18.66)
100	44.51	49.44 (37.69)	47.16 (34.22)	33.00 (30.65)	31.70 (28.50)	30.30 (24.85)
120	54.87	64.71 (48.40)	59.95 (43.48)	57.10 (41.20)	37.40 (31.73)	15.50 (12.02)
140	65.87	nil	70.85 (56.67)	60.78 (50.36)	20.80 (16.90)	12.80 (9.60)
160	76.50	83.31 (82.40)	89.99 (89.12)	52.93 (46.46)	15.00 (11.63)	11.99 (8.90)

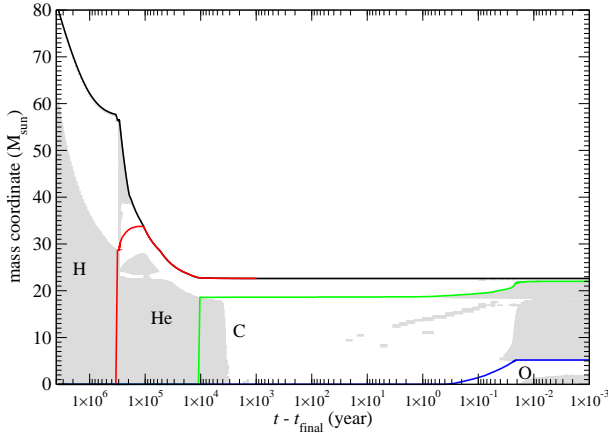


Figure 1. Kippenhahn diagram of the main-sequence of $M = 80 M_{\odot}$ at solar metallicity from the H-burning. The time stands for the time before the core reaches a temperature of $10^{9.4}$ K.

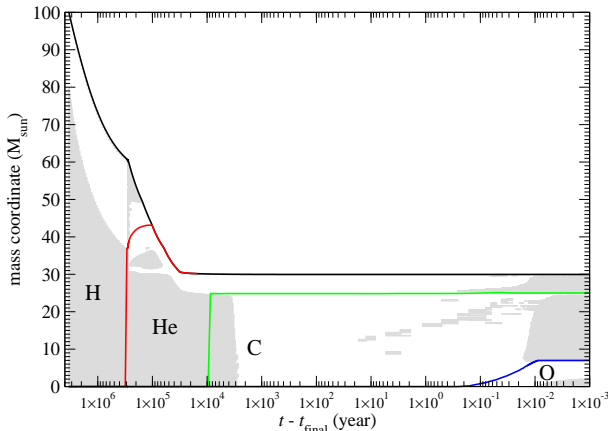


Figure 2. Similar to Figure 1, but for $M = 100 M_{\odot}$.

extremely large mass loss rate that half of the matter is lost in the helium burning phase for $M = 80$ and $100 M_{\odot}$. and in the hydrogen burning phase for $120 M_{\odot}$. The whole H envelope is lost during He-burning, which occurs about 10^5 year before collapse. The initial He core mass can reach about half of the initial mass, but it gradually decreases due to the later mass loss. Also, in all three models, after the removal of H-envelope or He-

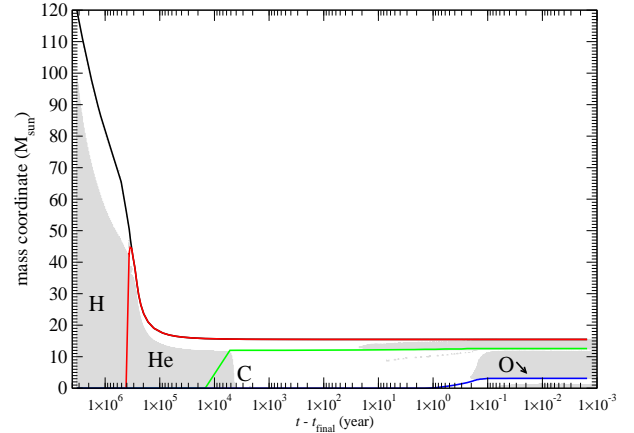


Figure 3. Similar to Figure 1, but for $M = 120 M_{\odot}$.

burning, the C-core quickly forms with a mass similar to the He-core mass. For 80 and $100 M_{\odot}$ models they have a C core mass $\sim 20 M_{\odot}$ which remains unchanged after it has been formed. The $120 M_{\odot}$ one has a somewhat smaller one due to the previous drastic mass loss.

The convective pattern of the star is consistent with typical massive stars. In H-burning phase, the core is mostly convective, while the surface is radiative. In the He-burning phase, the core remains convective while some H-envelope becomes convective. But this feature disappears when the mass loss sheds away the H-envelope. Once the C-core has formed at about 10^4 year before pulsation, the star begins to contract rapidly. The core becomes radiative. But together with the C-core and C-envelope burning, layers of convective shells appear. They gradually propagate and reach the C-core surface. When the core starts O-burning (10^{-1} year from the onset of first pulsation), the strong energy generation triggers large scale convection that the whole C-envelope becomes convective. The inner core of O-rich region also becomes convective.

In Figures 4, 5 and 6 we plot similar to the previous three figures but at $Z = 0.1 Z_{\odot}$. Different from the models at solar metallicity, the low metallicity implies low opacity in the matter, and thus lowers the mass loss during the H- and He-burning phase. There is a clear

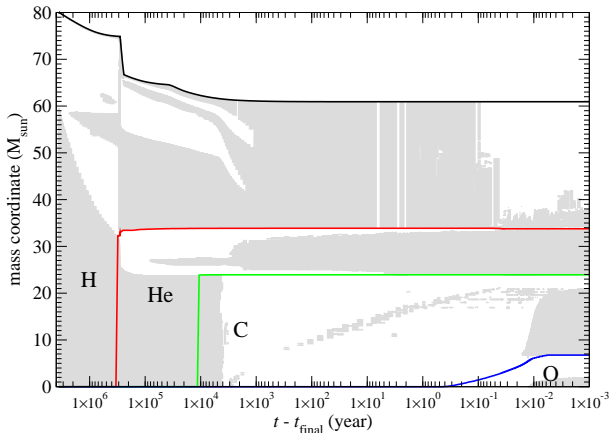


Figure 4. Kippenhahn diagram of the main-sequence of $M = 80 M_{\odot}$ at $0.1 Z_{\odot}$ from the H-burning until the core reaches a temperature of $10^{9.4}$ K.

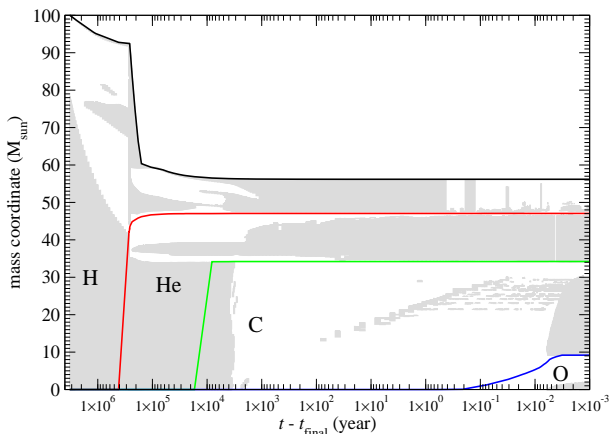


Figure 5. Similar to Figure 4, but for $M = 100 M_{\odot}$.

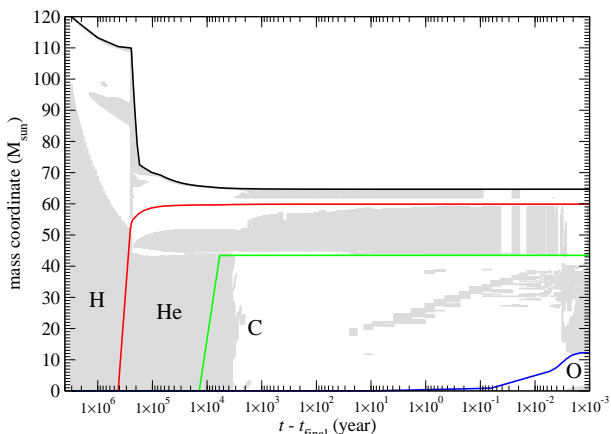


Figure 6. Similar to Figure 4, but for $M = 120 M_{\odot}$.

signature of massive He core from 30 to $50 M_{\odot}$. The He core mass remains constant after it has formed. Near the occurrence of first pulsation, a massive CO core $\sim 10 M_{\odot}$ is also formed. A generally larger O-rich core is formed at the end of simulation.

Due to the preservation of H-envelope after He-burning, the star consists of a rich structure of convection activities before its collapse. The convective core has a similar structure to the higher metallicity case, due to the extended H-envelope remained after He-burning, there is also a second convective zone which gradually move inward to the stellar core from its initial $60 M_{\odot}$ to $\sim 40 M_{\odot}$. After that the He-core is fully convective during He-burning and the convection zone extends into the H-envelope. The surface is also convective. During C-burning, the convective layer propagates outwards from the core to the C-core surface. The outer layers of He- and C- envelopes are convective. During contraction before the onset of O-burning, the core returns to be radiative dominated. Similar to the high metallicity case, near the onset of pulsation, the core becomes convective.

3.2. Pre-pulsation evolution

In the left panel of Figure 7 we plot the HR diagram for the main-sequence star models with $M = 80, 100, 120$ and $140 M_{\odot}$ included. All models are fixed at $Z = 0.002 Z_{\odot}$. For numerical stability we do not include mass loss for the $140 M_{\odot}$ model. In the pre-pulsation evolution, the models follow the typical HR diagram of main-sequence star, The H-burning occurs after the star has contracted. After H is exhausted, the star develops into red giant with He burning which largely increases its luminosity. Depending on the mass loss, the effective temperature can largely reduce. Also, the typical luminosity increases with mass.

In the right panel we plot the evolution of the central temperature against the central density for the same set of models. We also draw the pair-instability zone (defined by the adiabatic index $\Gamma < 4/3$). There is no intersection among models, showing that the thermodynamics properties of the core before pulsation depend on only its mass. The contraction of the core follows mostly adiabatic contraction (with a slope -3) in the diagram.

3.3. He Core and CO Core Mass Relations

To study the effects of metallicity and rotation, we perform pre-pulsation stellar evolution models for different metallicity from $Z = 10^{-3} Z_{\odot}$ up to $Z = 1 Z_{\odot}$ for non-rotating main-sequence star model. In Table 3 we tabulate the pre-pulsation configurations of the main-sequence stars for their He- and CO- core masses when

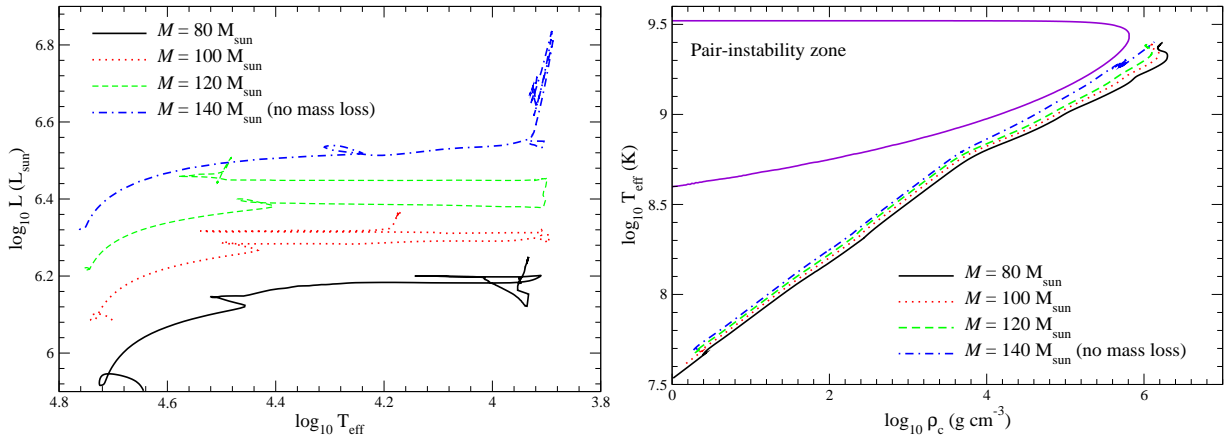


Figure 7. (left panel) The HR diagram of the main-sequence stars from 80 to 140 M_{\odot} . Notice that for the 140 M_{\odot} model no mass loss is assumed due to the later numerical instability. (right panel) Similar to the left panel, but for the T_c against ρ_c diagram. The zone enclosed by the purple curve corresponds to the instability zone defined by $\Gamma < 4/3$.

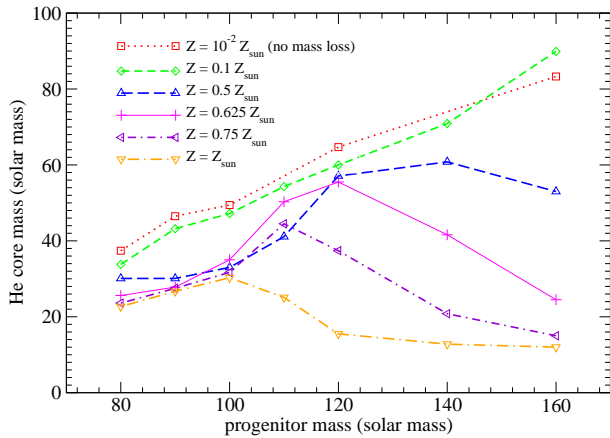


Figure 8. The He core mass against progenitor mass when the core exhausts its hydrogen for stellar models at different metallicity. For $Z = 10^{-2} Z_{\odot}$, the models assuming no mass loss is assumed because of numerical instability encountered during He-burning in the asymptotic red-giant branch.

the core exhausts all H and He respectively. The CO core masses are written in brackets.

He core mass grows monotonically with M when $Z < 0.625 Z_{\odot}$. For star models with a higher metallicity, the mass loss rate, which is proportional to the metallicity, makes the He core mass drop at the high mass end. This transition starts at a lower mass for models with a higher metallicity. Notice that the change and the transition mass is not linearly proportional to Z due to the non-linear dependence of mass-loss rate. Also, the mass loss affects the gravity, which changes the equilibrium structure of the star even in the H-burning phase.

In Figure 8 we also plot the relations He core mass against progenitor mass for different metallicity. On one hand, at low mass, the He core mass is not so sensitive to metallicity, that the He core mass approaches its asymptotic value when $Z \leq 10^{-2} Z_{\odot}$. On the other hand, at

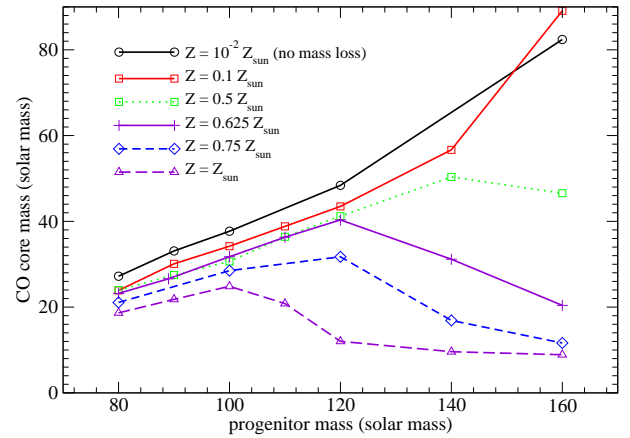


Figure 9. The C core mass against progenitor mass when the core exhausts its He for stellar models at different metallicity. Again, for $Z = 10^{-2} Z_{\odot}$ the models assume no mass-loss due to numerical instability.

high mass, the He core mass is very sensitive to metallicity that from $Z = 0.625 Z_{\odot}$ to $Z = Z_{\odot}$ the He core mass can drop by 90 % at the star model $M = 160 M_{\odot}$, about $15 M_{\odot}$. At such low mass, the He core already leaves the pulsation pair-instability regime, and evolves as a normal CCSN. Furthermore, the maximum He core mass for models at solar metallicity only barely reaches the transition mass $40 M_{\odot}$.

For models which completely covers the PPISN mass range (He star of mass 40 – 64 M_{\odot}), we require stellar model with a metallicity at most $0.1 Z_{\odot}$. This shows that the PPISN is very sensitive to the progenitor metallicity, while stars with solar metallicity are less likely to form PPISN owing to its mass loss.

Then we examine the CO core mass. Before the CO core mass can be defined, the massive CO core has already started its contraction, which increases the CO

core mass. The metallicity effect is a similar trend to the He core mass. In all models, at the lower mass branch CO core mass in general increases with progenitor mass, but it drops at the high mass end. The CO core mass also shows a monotonic decreasing relation against metallicity for the same progenitor mass. The mass loss effect in near solar metallicity models are more significant that the CO core mass contributes to less than 10 % of the stellar mass, while those with a lower metallicity can be about one third of the progenitor mass.

In Figure 9 we also plot the relation CO core mass against progenitor mass at different metallicity. The significance of the metallicity of mass loss rate can be seen. By increasing models from $0.5 Z_{\odot}$ to $0.75 Z_{\odot}$, the CO core mass can drop by 75 % at $M = 160 M_{\odot}$. The CO core mass shows a clearer relation than the He core mass. The mass scaled clearly with metallicity, except at $M = 160 M_{\odot}$, where the model without mass loss ($Z = 10^{-2} Z_{\odot}$) has a lower mass than its counterpart of $Z = 0.1 Z_{\odot}$.

4. PULSATONAL PAIR-INSTABILITY IN HELIUM STARS

In this section we study the evolution of PPISN using the zero-age He main-sequence as the initial condition. We consider stellar model with pure He, i.e. zero metallicity, as indicated that a massive He-core is likely to be form when $Z \leq 10^{-1} Z_{\odot}$. We do not evolve dynamically with H because the H-envelope is not tightly bounded by the gravitational well of the star. It is easily disturbed and obtains high velocity during shock outbreak. We find that to keep the H-envelope while evolving the whole star is computationally difficult. However, as the H-envelope does not couple strongly to the inner core, the pulsation dynamics is not significantly changed, when we do not consider the effects of H-envelope. Therefore, in this section, we consider the dynamics, energetics, mass loss and chemical properties of the PPISN by using the He-star as the initial condition. However, we notice that in general a He-star does not always one-one correspond to the He-core evolved from traditional stellar evolution. We also remark that the core masses for the major elements are defined by the mass coordinate where that particular element (or major isotope) reaches a mass fraction > 1 %. The convective mixing is switched off when we use the hydrodynamics option because of the numerical difficulties. In fact, the dynamical timescale can be shorter than mixing timescale when the shock has formed or dynamically expanding. It is unclear for those scenarios whether convection can be formed robustly. An incomplete mixing

model or time-dependent convection model is necessary for following this part of input physics.

4.1. Evolution in Kippenhahn Diagram

In this part we examine the overall evolution of the PPISN evolved from He core until the onset of Fe-core collapse.

In Figures 10 and 11 we plot the Kippenhahn diagram of Models He40A, He50A, He60A and He62A. The coloured zone is again the convective zone while the lines (solid, dotted, dashed, long-dash, dot-dash) are the He-, C-, O-, Si- and Fe-core mass coordinate. The x-axis is the time counting backward from its collapse. We define the core boundary to be the inner boundary of the mass fraction for that corresponding element to drop below 10^{-2} . Therefore, since we start from a He core, the He-rich surface, which is also the total mass of the star, stands for the He-core. Notice that for the cases with strong mass ejection, the whole He-rich surface can be shredded off. Here the time is defined by the remaining time from the onset of final collapse.

For Model He40A, after the strong pulsation, the star expands and the outer part of the star above $18 M_{\odot}$ becomes convective. Also, the star established its O- and Si-cores at $m(r) \sim 5 M_{\odot}$ and its Fe-core at $m(r) \sim 2 M_{\odot}$. Radiative transfer remains the major energy transport in the core. Thin layers of convection shells can be found in most parts of the He- and C-envelope. At about 10^{-1} year, the Si and O core can reach as far as $\sim 30 M_{\odot}$. This is because during the propagation of the acoustic wave near surface, the density gradient accelerates the wave into a shock, which heats up the matter around there. As a result, in such He-rich material, it facilitates the He-burning and gives product including C, O, Ne and Si. However, accompanied with the extended convection during the expansion-contraction phase, the outer O- and Si-rich zones disappear and the values correspond to the inner layers, which come from previous hydrostatic burning.

For Model He50A, after the pulsation, the C-, O- and Si-cores are produced simultaneously. But the O- and Si-cores quickly retreat from $30 M_{\odot}$ to 5 and $10 M_{\odot}$ respectively. The early formation of O- and Si-cores is because when the shock reaches the surface, the shock heating is capable in producing O- and Si-rich material around that region. However, away from the shock-heated zone, no significant O- and Si-productions take place. However, after the production, the mixing and mass loss by pulsation quickly remove these material. As a result, the O- and Si-core mass coordinates return to the corresponding inner values, where the real O- and Si-core locate. At 10^{-3} year before the final collapse, the

Table 2. The main-sequence star models prepared by the MESA code. M_{ini} and M_{fin} are the initial and final masses of the star. M_{H} , M_{He} , M_{CO} are the hydrogen, He- and CO-mass before the hydrodynamics code starts. All masses are in units of solar mass.

Model	M_{ini}	M_{fin}	M_{H}	M_{He}	M_{C}	M_{O}	remarks
He40A	40	40	0	6.79	3.13	27.5	only He core
He45A	45	45	0	7.38	4.03	31.3	only He core
He50A	50	50	0	7.82	4.16	35.2	only He core
He55A	55	55	0	8.27	4.30	39.0	only He core
He60A	60	60	0	8.69	4.43	42.9	only He core
He62A	62	62	0	8.77	4.59	44.6	only He core
63HeA	63	63	0	8.89	4.64	45.3	only He core
He64A	64	64	0	8.96	4.63	46.1	only He core

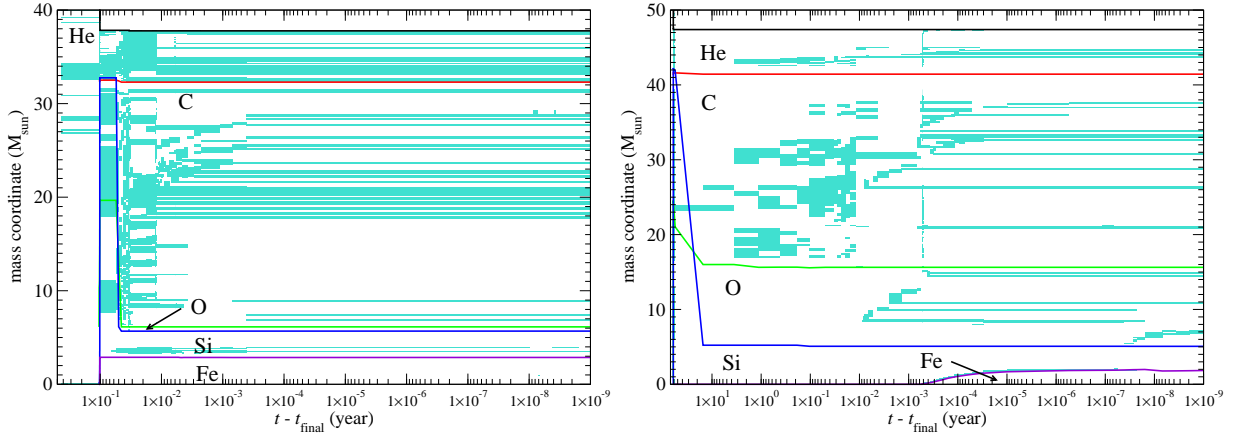


Figure 10. (left panel) Kipperhahn Diagram for the Model He40A ($M_{\text{He}} = 40 M_{\odot}$) until the onset of final collapse. The lines correspond to the inner boundary where the mass fractions of the respective elements drop below 10^{-2} . By this definition, the surface mass coordinate of the star, if it does not experience strong mass ejection, is the He-core mass since we start from a He-star. (right panel) Similar to Figure 10, but for $M_{\text{He}} = 50 M_{\odot}$. The time on the x-axis is defined by the time before the onset of final collapse.

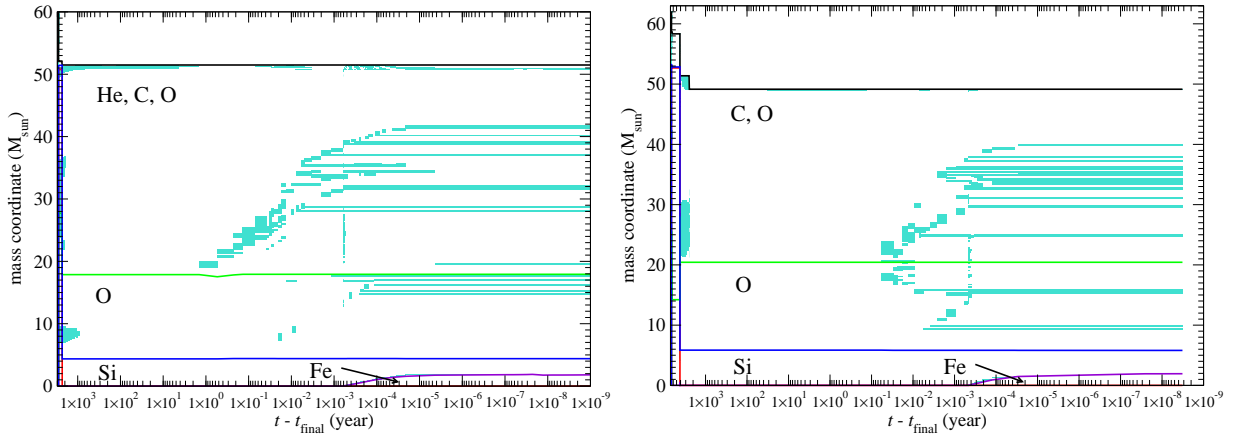


Figure 11. (left panel) Similar to Figure 10, but for $M_{\text{He}} = 60 M_{\odot}$. (right panel) Similar to Figure 10, but for $M_{\text{He}} = 62 M_{\odot}$.

contraction of star allows the central density to be high enough for burning until NSE. The Fe- and neutron-rich core forms almost simultaneously at $\sim 2 M_{\odot}$. Different from Model He40A, the inner core is no longer convective, except after pulsation. There is an extended period of time at $\sim 10^{-2}$ year before its final collapse, the star continues to hold fragmented convective layers.

For Model He60A, there is also no inner convective core after its pulsation. Again, the shock heating creates a temporary outer O- and Si-core outside surface, but they return to the inner ones after mass ejection and mixing, to ~ 5 and $15 M_{\odot}$. Different from the previous two models, the expanded star after pulsation does not reach any convective state before its second pulse or final collapse. An outward propagating convective structure can be seen from ~ 1 year before collapse. It moves from $m(r) = 20 M_{\odot} - 40 M_{\odot}$. The convection zone is small that it does not contribute in bringing the fuel from outer layer to the actively burning layer. Similar to Model He50A, the Fe- and neutron-rich cores appear at $\sim 2 M_{\odot}$ at 10^{-3} year before collapse.

For Model He62A, it is different from the previous three models because of its extensive mass loss after pulsation. After the first pulse, the star reaches a very extended period $\sim 10^4$ years of fully convective state. Again, the convection washes away the external C- and O-envelope. The first pulse creates a final C-, O-cores which locate at 20 and $5 M_{\odot}$ respectively. In the second pulsation, the Fe-core is also produced which has a mass $\sim 3 M_{\odot}$. During its contraction at 1 year before its final collapse, the core reaches the third convective state. During contraction, the outer extended convective zone also moves outward from 20 to $40 M_{\odot}$. The convective structure is again fragmented. A $2 M_{\odot}$ Fe-core is formed only near 10^{-3} year before the final collapse.

4.2. Pre-Pulsation Evolution

We first present the results for the pre-collapse profile based on the He main-sequence star in Table 2. The pre-pulsation evolution uses the hydrostatic approximation and it is done until the central temperature reaches $10^{9.4}$ K, where the dynamical timescale begins to be comparable with the O-burning timescale. Below $10^{9.3}$ K the star evolves in a quasi-static manner but not assuming hydrostatic equilibrium. From the table we can see that the initial He core mass affects the pre-pulsation C- and O- core. We choose the He-core models with a mass from 40 to $64 M_{\odot}$, which produce CO cores from 30.82 to $50.42 M_{\odot}$, with the remaining unburnt He in the envelope.

In Figure 12 we present the initial model profile and its composition. We find that most models are very

similar with each other, so for demonstration we picked $M_{\text{He}} = 60 M_{\odot}$ as an example. The star consists of three parts: A slowly varying core which extends up to $50 M_{\odot}$, an envelope of rapidly falling density and a surface with rapidly falling temperature.

In the right panel we plot the chemical abundance profile for the same model. The model contains a flat core of mostly ^{16}O up to $\sim 50 M_{\odot}$. Then it becomes C-rich and then He-rich until the surface of the star.

4.3. Pulsation

We first study the time evolution of the pulsation. To do so, we examine the second pulse of Model He60A, which is a strong pulse (with mass ejection) of mass $\approx 10 M_{\odot}$. We choose this particular pulse because it is strong enough to create global change in the profile so that we can understand the changes during the contraction (before maximum of central temperature in the pulsation) and expansion (after minimum of that in the pulsation) phases.

The core is mostly supported by the radiation pressure. With the catastrophe in pair production, the supporting pressure suddenly drops, where the core softens with corresponding equation of state adiabatic index $\gamma < 4/3$ in the core. However, unlike the stars with a mass $10 - 80 M_{\odot}$ which have rich Fe-cores at the moment of their collapse, in PPISN and PISN the core is mostly made of ^{16}O when contraction starts. The softened core allows a very strong contraction and the ^{16}O -rich core can reach the explosive temperature which releases a large amount of energy, sufficient to disrupt the star. ^{28}Si and ^{56}Ni can be produced during the contraction, where the central temperature can reach beyond $10^{9.5}$ K. As a result, the star stops its contraction and expands. The rapid expansion causes strong compression to the matter on the surface, which efficiently causes ejection of high velocity matter on the surface and dissipates the energy. After that, the core becomes bounded again. The pulsation restarts after it has lost most of its previously produced energy by radiation and neutrinos. The whole process repeats until the ^{56}Fe core, formerly ^{56}Ni , exceeds the Chandrasekhar mass that it collapses by its own gravity before the compression heating can reach the further outgoing ^{16}O -rich envelope.

In Figure 13 we plot in the top left, top right and middle left panels the temperature, density and velocity evolution at selected time respectively. We pick the profiles when the core temperature reaches $10^{9.3}$, $10^{9.4}$ and $10^{9.5}$ K before the core reaches its peak temperature during the pulse for Profiles 1-3, at its peak temperature for Profile 4, and after the core has reached its peak temperature for Profile 5 – 7 for the same central temperature

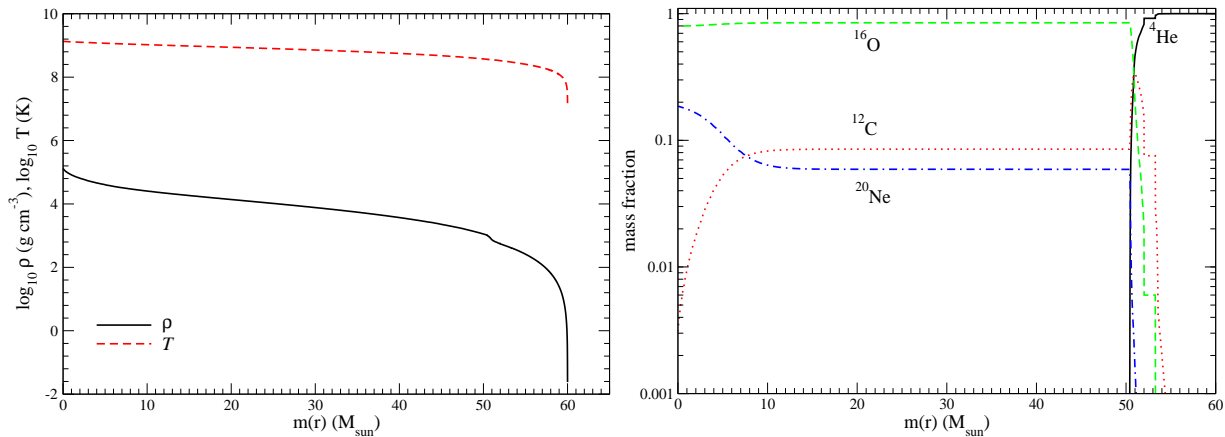


Figure 12. (left panel) The initial profile of density and temperature of Model He60A. (right panel) Similar to the left panel, but for the chemical composition including ${}^4\text{He}$, ${}^{12}\text{C}$, ${}^{16}\text{O}$ and ${}^{20}\text{Ne}$.

interval. In the middle right, bottom left and bottom right panels we plot the chemical abundance profiles for isotopes ${}^{16}\text{O}$, ${}^{28}\text{Si}$ and ${}^{56}\text{Ni}$ respectively.

First we study the hydrodynamics quantities. For the temperature, in the contraction (expansion) phase the star shows a global heating (cooling) due to the compression (expansion) of matter, and no temperature discontinuity can be observed. This shows that the whole star contracts adiabatically, without producing explosive burning in the star. By comparing the temperature profiles at the same central temperature (Profiles 1 and 7 for $T_c = 10^{9.3}$ K, profiles 2 and 6 for $T_c = 10^{9.4}$ K and profiles 3 and 5 for $T_c = 10^{9.5}$ K), the net effect of nuclear burning can be extracted. The part outside $q \sim 0.3$ has a higher temperature after the pulse. Similar comparison can be carried out for the density profile. The inner core within $q \sim 0.3$ is unchanged after pulsation, while the density in the outer part increases. The velocity profiles show more features during the pulse. Before the star reaches its maximally compressed state, the velocity everywhere is much less than 10^8 cm s $^{-1}$. At the peak of the pulse, the envelope has the highest infall velocity of $\sim 2 \times 10^8$ cm s $^{-1}$. After that, in Profile 5, the core starts the homologous expansion phase, with a sharp velocity discontinuity peak near the surface between the outward going core matter and the infalling envelope. Beyond Profile 6, the discontinuity reaches the surface and creates a shock breakout. The surface matter can freely escape from the star.

For the chemical composition, the effects of the pulse becomes clear. Since the second pulse, part of the core ${}^{16}\text{O}$ is already consumed in the first pulse, which is converted to ${}^{28}\text{Si}$ already. During the compression, before the core reaches its maximum temperature, ${}^{16}\text{O}$ is significantly consumed and forming ${}^{28}\text{Si}$. When the core reaches the peak temperature, the O within $q \approx 0.06$

is completely burnt, where intermediate mass elements, such as ${}^{28}\text{Si}$, is produced. However, Fe-peak elements, such as ${}^{56}\text{Ni}$ are not yet produced. On the other hand, during the expansion phase, most O-burning ceased, making the ${}^{16}\text{O}$ and ${}^{28}\text{Si}$ unchanged after the central temperature reaches $10^{9.4}$, while advanced burning still proceeds slowly to form Fe-peak elements.

4.4. Global Properties of a Pulse

Here we study some representative models of He core with a mass from 40 to $62 M_\odot$. They show very different pulsation histories, by their number of pulses and their corresponding strengths. In Table 4.4 we tabulate the stellar mass and the element mass in the star after each of the pulse.

For Model He40A, most of the pulses are weak, however, following each of the pulse, mass of ${}^{16}\text{O}$ is gradually consumed and produce ${}^{28}\text{Si}$. At late pulses, where the core reaches beyond 10^7 g cm $^{-3}$, NSE elements are also produced. In the last pulse, the core is sufficiently compressed such that an Fe core beyond $1.4 M_\odot$ is produced, which is followed by later mass loss. Most of the ejected mass is He.

For Model He45A, most of the pulses are weak. With the number of pulses increases, not only Si, but also ${}^{56}\text{Ni}$ are produced. The last pulse, which is the strongest overall, produces about $0.56 M_\odot$ Ni, while the generated heat creates a shock to eject about $6 M_\odot$ matter before the final collapse.

For Model He50A, the number of pulses becomes smaller and again only the last pulse is a strong pulse which can eject mass. Compared to previous models, in each pulse more ${}^{16}\text{O}$ is consumed, which produces Si. At the final strong pulse, less Ni is produced, while the accompanying mass loss ejects the He in the envelope. It should be noted that its lower mass ejection compared to Model He45A comes from the difference that the O in

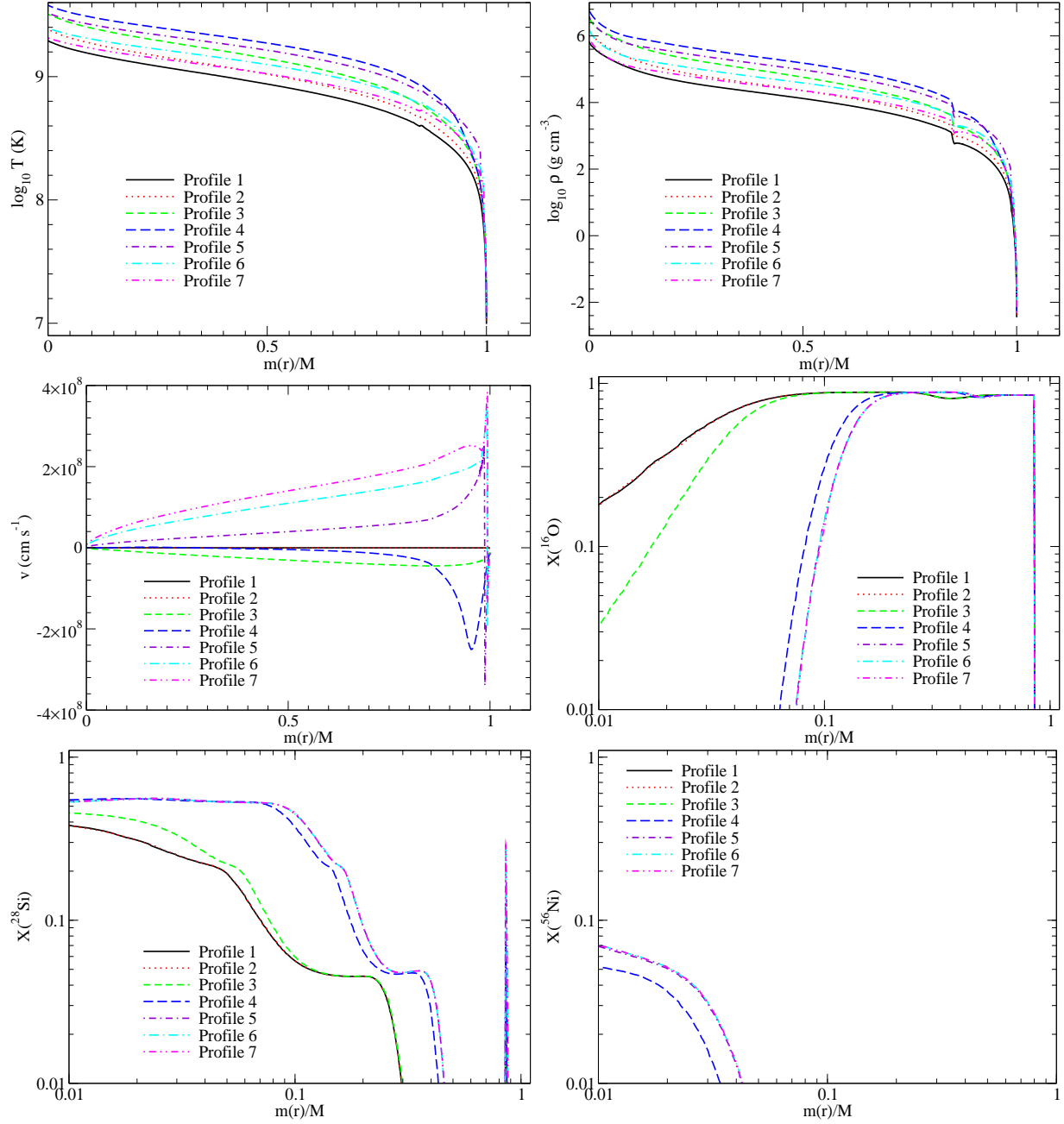


Figure 13. (top left) The temperature evolution of Model He60A around the second pulse. The profiles are chosen in the way that the central temperature reaches $10^{9.3}$ (Profile 1), $10^{9.4}$ (Profile 2), $10^{9.5}$ (Profile 3) before the pulse, during the peak (Profile 4), and the central temperature returns to $10^{9.5}$ (Profile 5), $10^{9.4}$ (Profile 6) and $10^{9.3}$ K (Profile 7) respectively. (top right) Similar to the upper left panel, but for the density profiles. (middle left) Similar to the upper left panel, but for the velocity profiles. (middle right) Similar to the upper left panel, but for ^{16}O mass fraction. (bottom left) Similar to the upper left panel, but for ^{28}Si mass fraction. (bottom right) Similar to the upper left panel, but for ^{56}Ni mass fraction.

Model He45A is burnt in a much compressed state. This creates a much stronger pulsation when the expansion approaches the surface, which increases the mass loss.

For Model He55A, it has two strong pulses, in contrary to lower mass models having only one strong pulse. Its pulses are qualitatively similar to Model He50A.

For Model He60A, it has no weak pulse. The contraction always makes a significant mass of O to be burnt to produce the thermal pressure to support the softened core against its contraction. Due to the strong mass ejection, at the end of the simulation the star almost runs out of He. However, one difference of this model from the others is that it has a much lower Ni mass after pulsation. Most of the Fe, which leads to the collapse, is created during the contraction towards collapse.

For Model He62A, it has a similar pulse pattern as Model He60A but is stronger. Each pulse can consume about $3 - 4 M_{\odot}$ of O. Different from previous models, Model He62A has an abundant amount of O even during its contraction towards collapse, and O continues to be consumed before it collapses.

For Model He64A, which is a pair-instability supernova instead of PPISN, there is only one pulse before its total destruction. Due to its much lower density when large-scale O-burning occurs, even when about a few solar mass of O is burnt during the pulse, the energy is sufficient to eject all mass when the pulse reaches the surface.

4.5. Thermodynamics

In Figures 14, 15 and 16 we plot the central density and temperature against time for Models He40A, He45A, He50A, He55A, He60A and He62A in the six panels respectively. To show that the rapid contraction comes from the PPI, we show in each plot the zones where electron-positron pair creation, the dynamical instability induced by photo-disintegration of matter in NSE at $Y_e = 0.5$ (Ohkubo et al. 2009) and the dynamical instability induced by general relativistic effects (Osaki 1966). The arrows in the figure show where the pulses take place. Here we define weak and strong pulse to the pulsation of the star without or with mass ejection. The strength of the pulse is further defined by how much the core expands and cools down.

For Model He40A, at the beginning the central density is the highest among all six models. It has thus weaker pulses because the core is more compact and degenerate. It has five weak pulses and one strong pulse (indicated by arrows in the figure) where each of the small pulses only leads to a small drop of the central density and temperature. Then the core quickly resumes its contraction again. Only at the final pulse, when the core begins

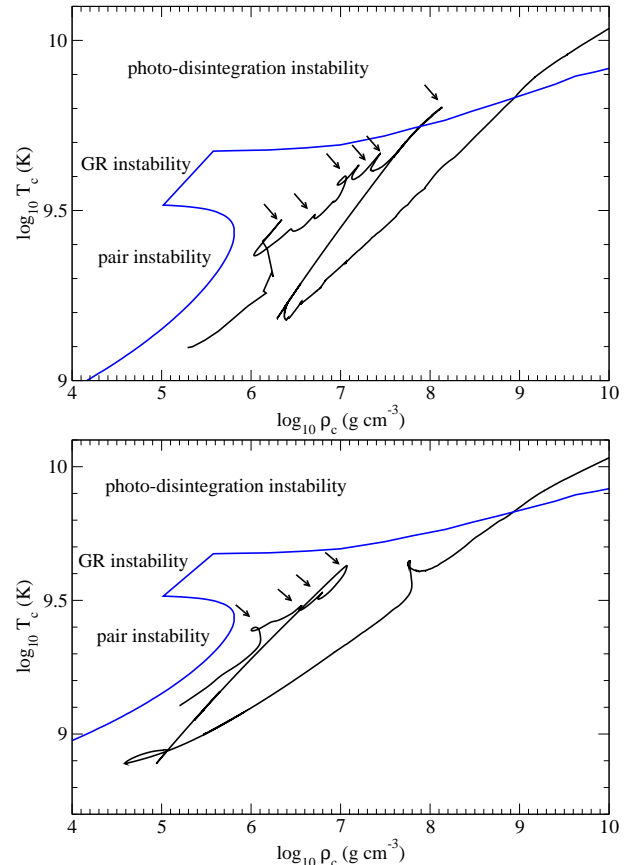


Figure 14. (*cont'd*) (upper panel) The central temperature against central density for Model He40A. (lower panel) Similar to the upper panel, but for Model He45A. In each plot, the region on the left of the blue line stands for regimes dominated by the dynamical instability of pair creation, general relativistic effects (see, e.g., Osaki (1966)) and photo-disintegration of matter in NSE at $Y_e = 0.5$ (Ohkubo et al. 2009). The arrows indicate where the pulsations take place.

to reach the Fe photo-disintegration zone, the softened core leads to a fast contraction and reaches a central temperature $T_c = 10^{9.8}$ K. This triggers a large scale O-burning in the outer core, which leads to a drastic drop in the central density and temperature, showing that the star is expanding, until the T_c reaches $10^{9.2}$ K. Then the core resumes its contraction. Since most O in the core is burnt, the Si-burning cannot produce adequate energy to create further pulsations. The star directly collapses.

For Model He45A, it shows a fewer number of pulses than Model He40A. It has three weak pulses and one strong pulse. The initial path is closer to the PC instability zone. The last pulse is triggered at $T_c = 10^{9.7}$ K and has a lowest T_c of $10^{8.9}$ K when it is fully expanded.

For Model He50A, it has only two weak pulses and one strong pulse. The evolution shows less structure compared to the previous two models because of the earlier

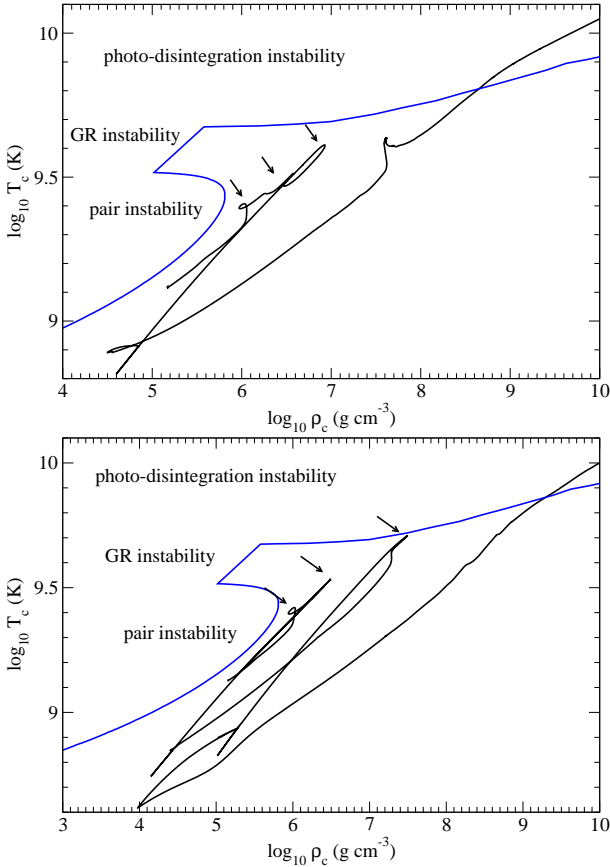


Figure 15. (*cont'd*) (upper panel) The central temperature against central density for Model He50A. (lower panel) Similar to the upper panel, but for Model He55A. The blue lines and the arrows follow the same meaning as in Figure 14.

trigger of large-scale O-burning in the core. The core starts the big pulse when $T_c = 10^{9.6}$ K and its expansion makes T_c reaching $10^{8.8}$ K at minimum. Before its collapse, there is a small wiggle along its trajectory. We notice that at this phase the core has a small pulsation when the core becomes degenerate.

For Model He55A, it has one weak pulse and two strong pulses. The two strong pulses start when T_c reaches $10^{9.5}$ and $10^{9.7}$ K respectively, with a minimum temperature after relaxation at $10^{8.8}$ and $10^{8.6}$ K.

For Model He60A, there is no weak pulse and two strong pulses, where the stellar core intersects with the PC instability zone during its expansion. The two pulses start when T_c reaches $10^{9.4}$ and $10^{9.6}$ K. The core finishes its expansion when it reaches $10^{9.0}$ and $10^{8.3}$ K.

For Model He62A, the star model becomes very close to the PC instability where the core enters the zone for a short period of time during its expansion. It is similar to Model He60A that there are two strong pulses. The two peaks start at $10^{9.5}$ and $10^{9.7}$ K while both pulses end at a minimum temperature of $10^{8.4}$ K, showing that

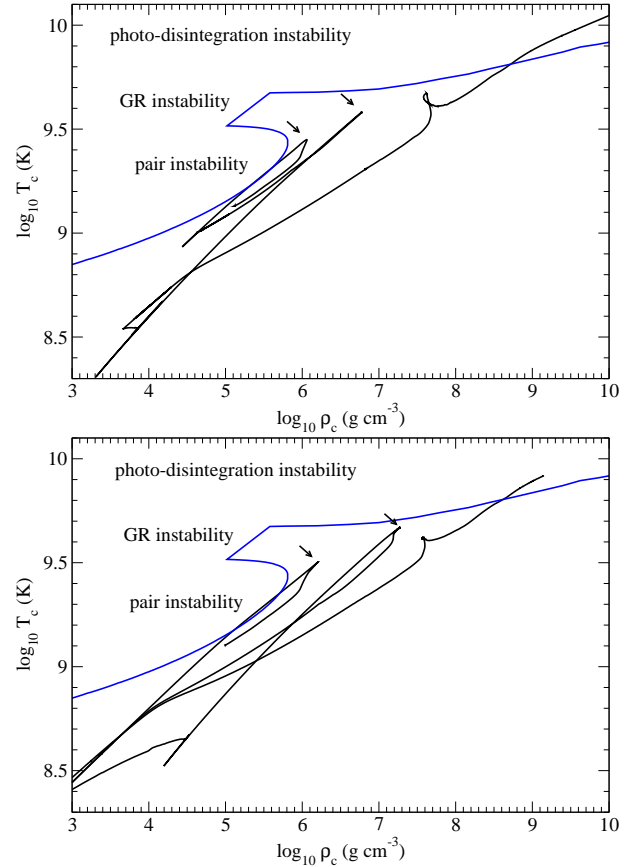


Figure 16. (*cont'd*) (upper panel) The central temperature against central density for Model He60A. (lower panel) Similar to the upper panel, but for Model He62A. The blue lines and the arrows follow the same meaning as in Figure 14.

the two pulses are of similar strength. After that, the core starts collapsing similar to all other five models.

By comparing all six models, we can observe the following trend for the pulse structure as a function of progenitor mass. First, when the progenitor mass increases, the number of small pulses decreases while the number of big pulses increases. Second, the strength of the big pulses increase with the progenitor mass, which leads to a lower central temperature and density during its expansion. Third, the path during its early pulses becomes closer to the PC instability as mass increases. Fourth, the second strong pulse strength is stronger than the first strong pulse.

4.6. Energetics

In Figures 17, 18, and 19 we plot the energy evolution for Models He40A, He45A, He50A, He55A, He60A and He62A, including the total energy E_{total} , internal energy E_{int} , gravitational energy E_{grav} and kinetic energy E_{kin} . The energy is scaled in order to make the comparison easier.

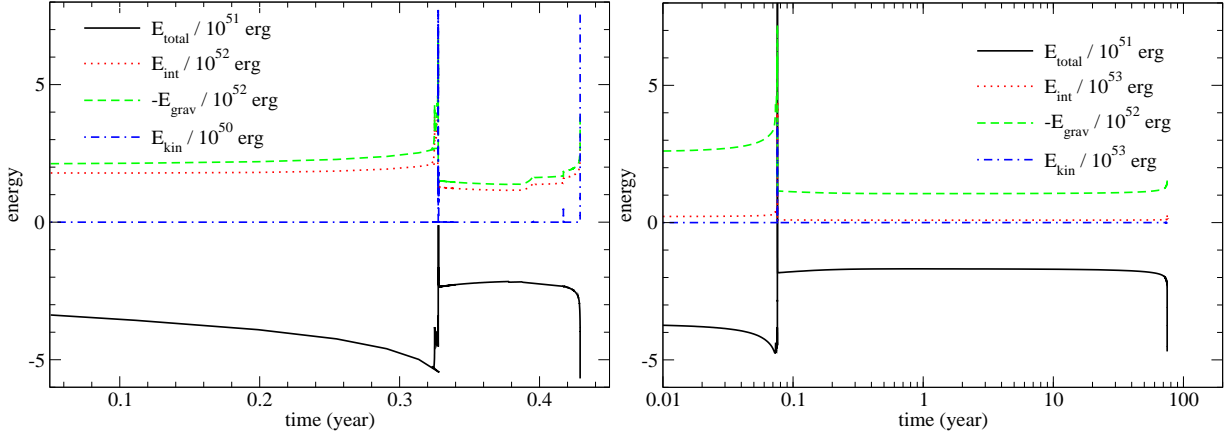


Figure 17. Total E_{total} , internal E_{int} , net gravitational E_{grav} and kinetic E_{kin} energies against time for Models He40A (left panel) and He45A (right panel) respectively.

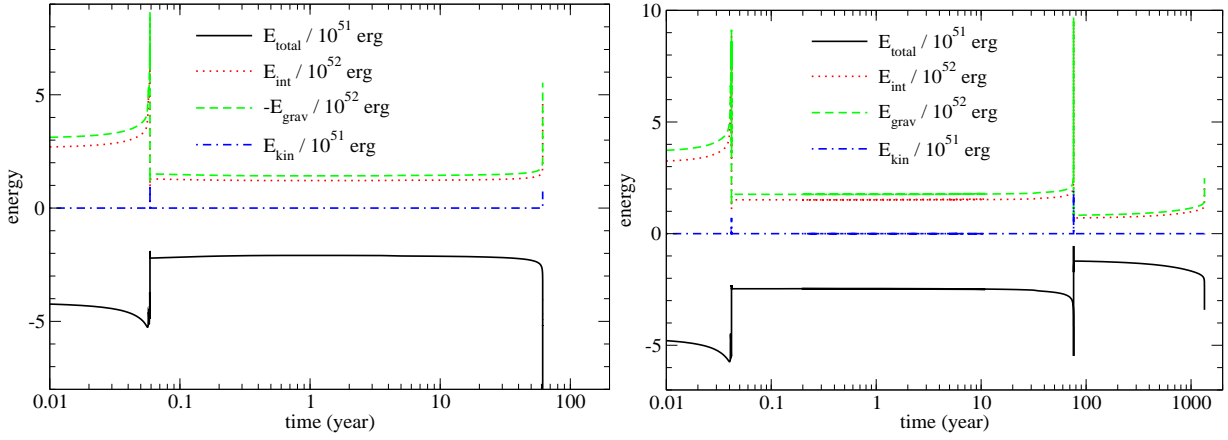


Figure 18. Similar to Figure 17, but for Models He50A (left panel) and He55A (right panel) respectively.

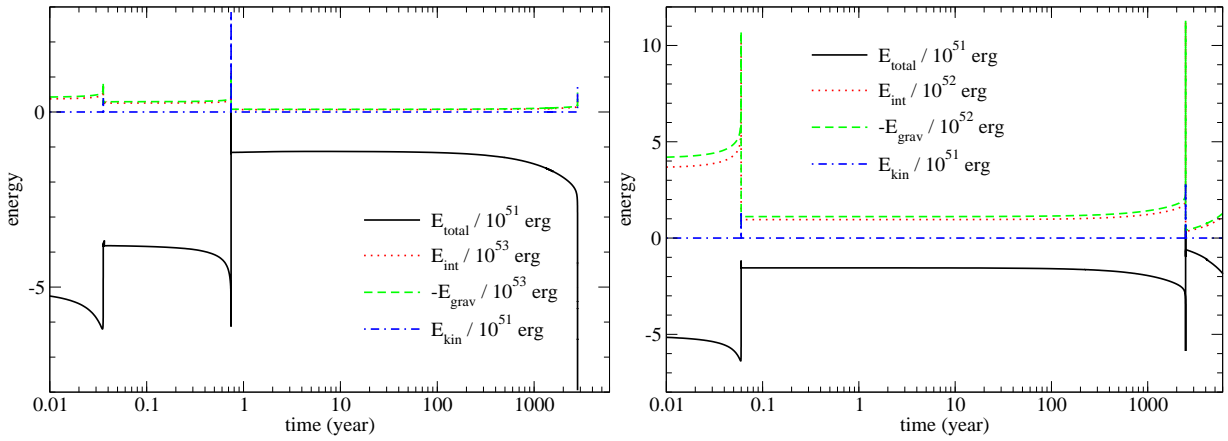


Figure 19. (*cont'd*) Similar to Figure 17 but for Models He60A (left panel) and He62A (right panel) respectively.

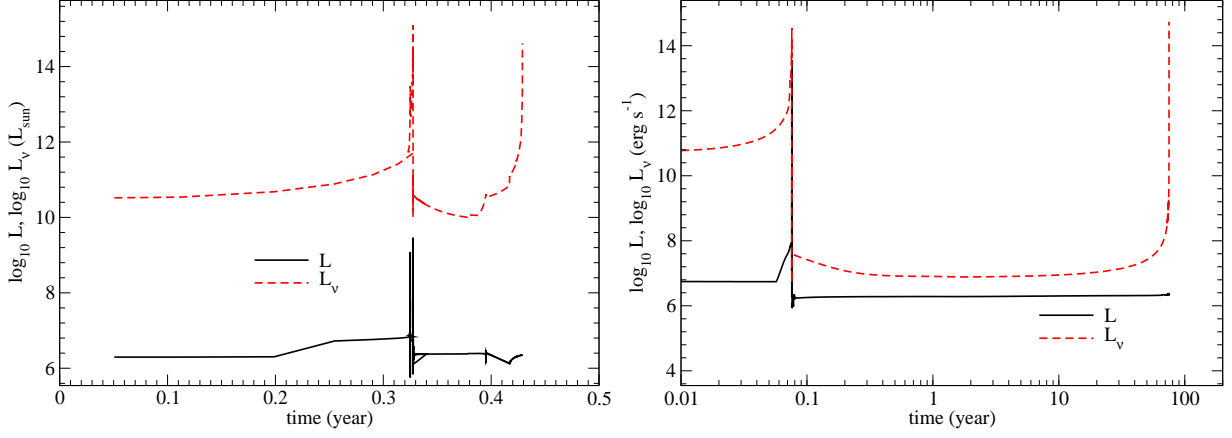


Figure 20. Total luminosity and neutrino luminosity against time for Models He40A (left panel) and He45A (right panel) respectively.

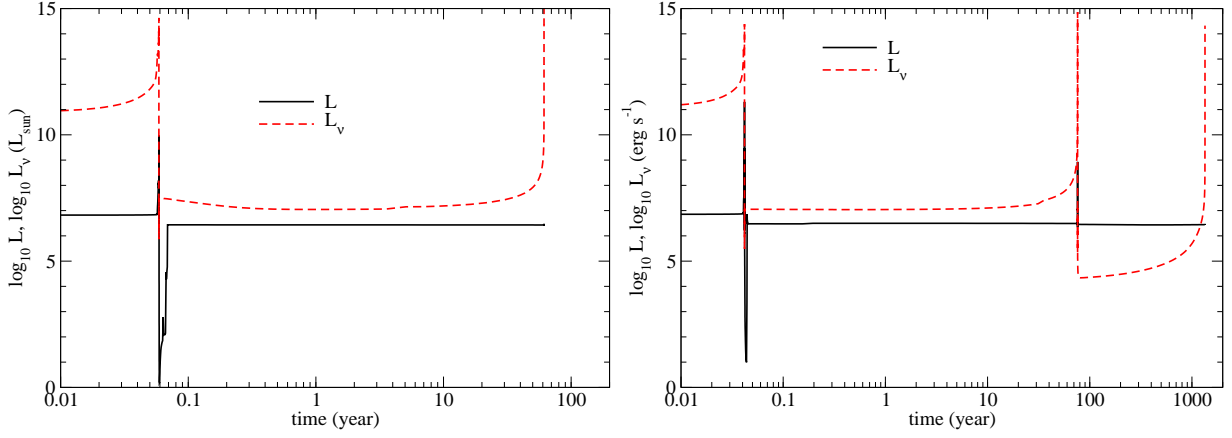


Figure 21. Similar to Figure 20, but for Models He50A (left panel) and He55A (right panel) respectively.

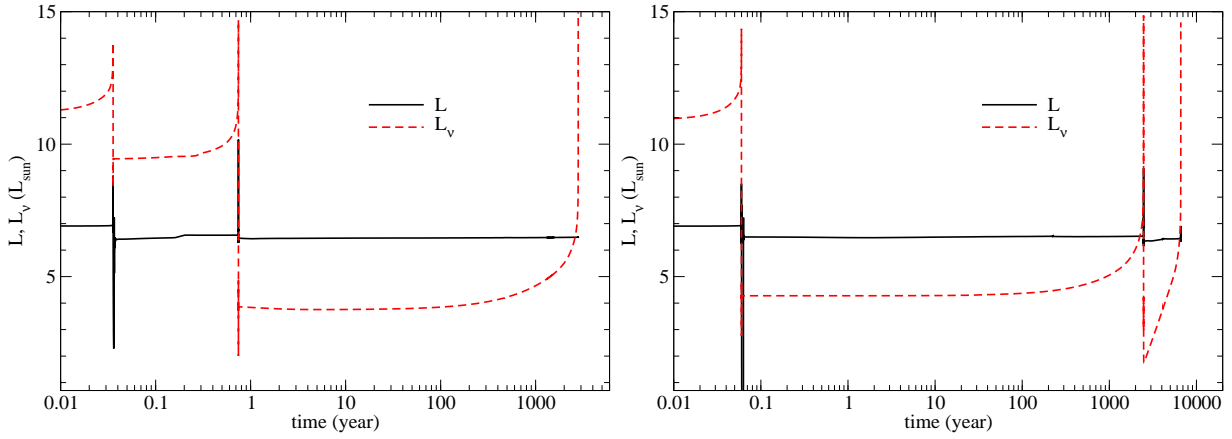


Figure 22. Similar to Figure 20, but for Models He60A (left panel) and He62A (right panel) respectively.

In all six models, the energy evolution does not depend on the stellar mass strongly, except for the energy scale. In all these models, the small pulses do not make observable changes in the energy except for very small wiggles. The contraction before a pulse leads to a denser and hotter core, where neutrino emission continuously draws energy from the system. At a big pulse, the total energy shows a rapid jump which increases close to zero, then the ejection of mass quickly removes the generated energy, making the star bounded again. Similar jumps in E_{int} and E_{grav} show that the core is strongly heated due to contraction heating and nuclear reactions. After that, the star reaches a quiescent state with a mild increase of total energy due to the ^{56}Ni decay, then followed by a quick drop when it contracts again.

4.7. Luminosity

In Figures 20, 21 and 22 we plot the luminosity evolution for the six models similar to Figure 17. During the pulse, the extra energy from nuclear reactions allows the luminosity to grow by 3-4 orders of magnitude. For a short period of time ($\leq 10^{-2}$ year), then the star becomes dim suddenly. After that the star resumes its original luminosity quickly and remains unchanged until the next pulse or final collapse. We remind that the luminosity during shock breakout and shortly after it cannot be trusted because it requires in general non-equilibrium radiative transfer for an accurate treatment.

The neutrino luminosity is more sensitive to the structure of the star. The neutrino luminosity can also jump by 3 – 10 orders of magnitude from its typical luminosity in the hydrostatic phase to the maximally compressed state. After the star has relaxed, the neutrino luminosity drops drastically. Depending on the strength of the pulse, neutrino cooling can become unimportant in the quiescent phase.

4.8. Mass Loss History

During the pulsation, when the bounce leads to the explosive burning in the core and inner envelope, sufficient energy is produced to create an outgoing shock, where the outermost matter can gain sufficient energy to be ejected from the star. The ejected matter later cools down and becomes the circumstellar matter (CSM). The existence of such H-free CSM is necessary in the circumstellar interaction models for Type I superluminous supernovae (SLSNe-I) (Sorokina et al. 2016; Tolstov et al. 2017). The chemical and hydrodynamics properties of the CSM thus become important, which influence the formation of the light curve of the explosion.

In Table 4.8 we tabulate the mass loss history of each model and its chemical composition. In Figures 23, 24,

25 and 26 we plot the ejecta profiles of the representative pulsation taken from Models He40A, He50A He60A and He62A respectively. Three patterns can be observed in the mass ejection. We choose these models because these examples characterize the typical ejecta features of strong pulses in the lower and higher mass regimes. We take the numerical values when the mass shells are ejected during the pulsation because that is the last moment the code keeps track of their evolution.

The first group is the strong pulse in the lower mass branch. In Models He40A and He45A the last pulse is the pulse which ejects mass. It shows wiggles in its density profiles, showing that the thermal expansion creates the first wave of mass ejection, followed by the shock as the velocity discontinuity approaching the surface, which creates the second wave of mass ejection. In both cases, only the He layer is affected, but as the He layer becomes thin, matter near the CO layer is ejected.

The second group is the weaker pulse of the more massive branch. In Models He50A, He55A He60A and He62A the first strong pulse occurs after the core starts to consume O collectively. Since it burns much less O than other strong pulses, the ejection comes from the rapid expansion of the star, which includes matter in the He envelope.

The third group is the strong pulse of the more massive branch. In Models He55A and Model He60A, the second pulse is stronger so that the ejecta density gradually decreases. A continuous ejection of mass in terms of smooth density profile is found. The mass ejection is sufficient deep that at the end of pulsation, traces of ^{12}C and ^{16}O can be found. We remark that the inclusion of massive elements (compared with H and He) will be important for the future light curve modelling because they contribute as the main source of opacity.

One of the pulsations needs to be discussed separately because of its very massive mass ejection, which involves very unique chemical composition in its ejecta. In Model He62A (right plot), the second pulse becomes strong enough that, besides its decreasing density profile, the later ejected material contains a significant amount of heavier elements including C, O, Mg and Si, showing that the He envelope is completely exhausted before the star is sufficiently relaxed.

4.9. Chemical Properties

In Figures 27, 28, 29 and 30 we plot the isotope profiles at different moments of selected Models He40A, He50A, and He62A. We selected moments before and after each strong pulse to extract the nuclear burning history. The models are chosen to demonstrate how different strength of pulsation and its convective mixing between pulses

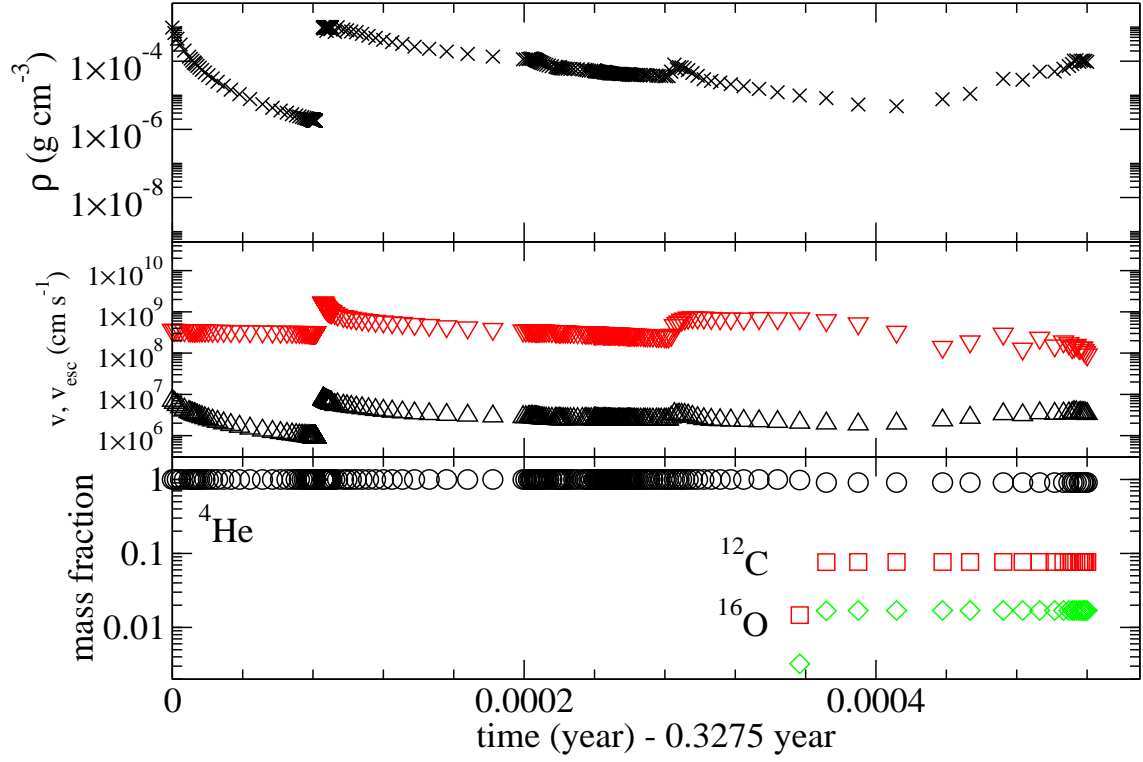


Figure 23. The mass ejection history of Model He40A, including in the upper panel the ejecta density, in the middle panel the ejecta velocity and the escape velocity and in the lower panel the ejecta chemical composition.

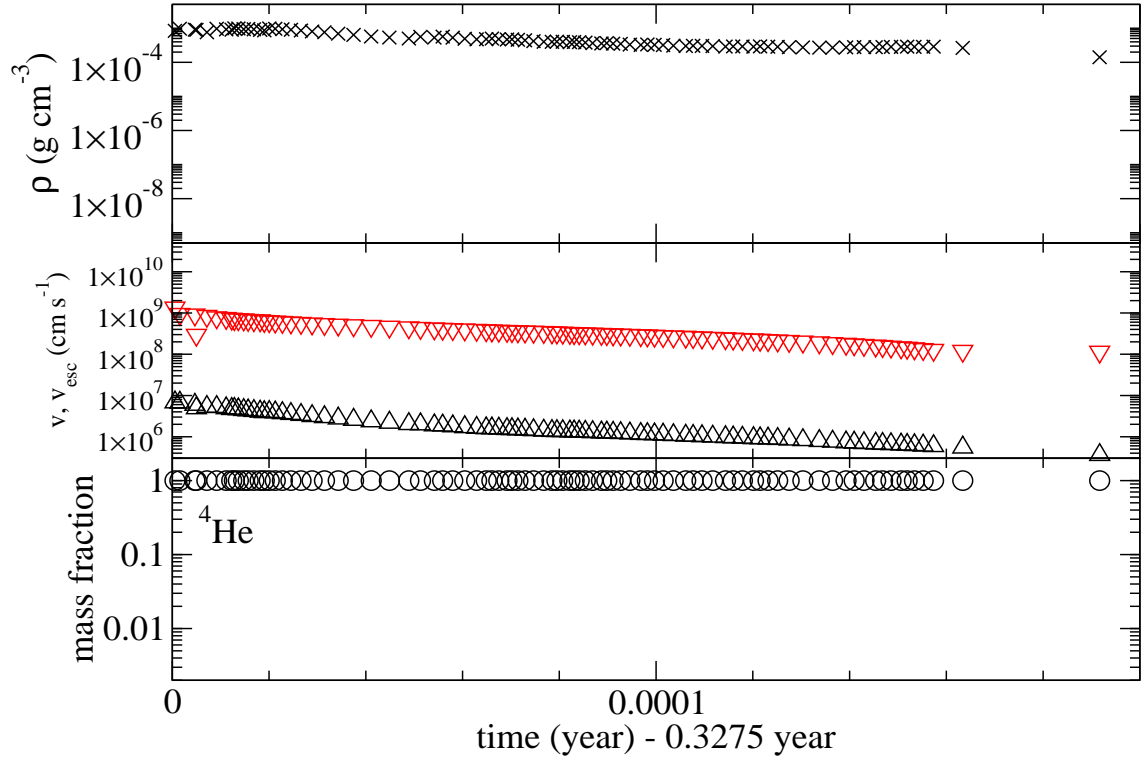


Figure 24. (*cont'd*) The mass ejection history of Model He50A including the density (top panel), velocity (middle panel) and chemical composition (bottom panel). For the velocity plot, the black triangles and red inverted triangles correspond to the ejecta and escape velocities at the surface.

Table 4. Energetic and chemical composition of the ejecta. 'Pulse' stands for the sequence of pulses in its evolution. 'Time' is the occurrence time in units of year. T_{ej} is temperature range of the ejecta in units of K. E_{ej} is the ejecta energy in units of 10^{50} erg. $M(\text{He})$, $M(\text{C})$, $M(\text{O})$, $M(\text{Ne})$, $M(\text{Mg})$, $M(\text{Si})$ are the masses of He, C, O, Ne, Mg and Si in the ejecta in units of solar mass.

Model	Pulse	time	M_{ej}	E_{ej}	T_{ej}	$M(\text{He})$	$M(\text{C})$	$M(\text{O})$	$M(\text{Ne})$	$M(\text{Mg})$	$M(\text{Si})$
He40A	6	9.9×10^{-2}	1.0	1.0	6.3-6.8	1.0	0.0	0.0	0.0	0.0	0.0
He45A	1	7.4×10^{-2}	4.0	6.6	6.5-6.9	3.8	0.2	0.0	0.0	0.0	0.0
He50A	2	2.0×10^{-1}	4.0	2.5	6.7-7.2	3.9	0.1	0.0	0.0	0.0	0.0
He55A	1	6.2×10^{-2}	0.3	1.8	6.8-7.1	0.3	0.0	0.0	0.0	0.0	0.0
He55A	2	1.9	10.0	13.1	6.0-6.7	7.5	1.0	0.8	0.2	0.3	0.2
He60A	1	1.7×10^{-1}	10.6	5.1	5.3-6.4	8.6	2.4	0.8	0.6	0.2	0.2
He60A	2	7.4×10^3	38.7	59.0	6.0-6.5	0.0	1.1	32.5	1.3	1.3	2.0
He62A	1	5.5×10^{-2}	0.6	0.1	6.8-7.4	0.6	0.0	0.0	0.0	0.0	0.0
He62A	1	3.5×10^3	55.4	29.6	4.6-7.2	7.8	1.7	33.2	1.6	1.8	5.8
He64A	1	4.9×10^{-2}	21.8	29.4	4.4-7.1	8.5	1.8	9.9	0.9	0.3	0.6

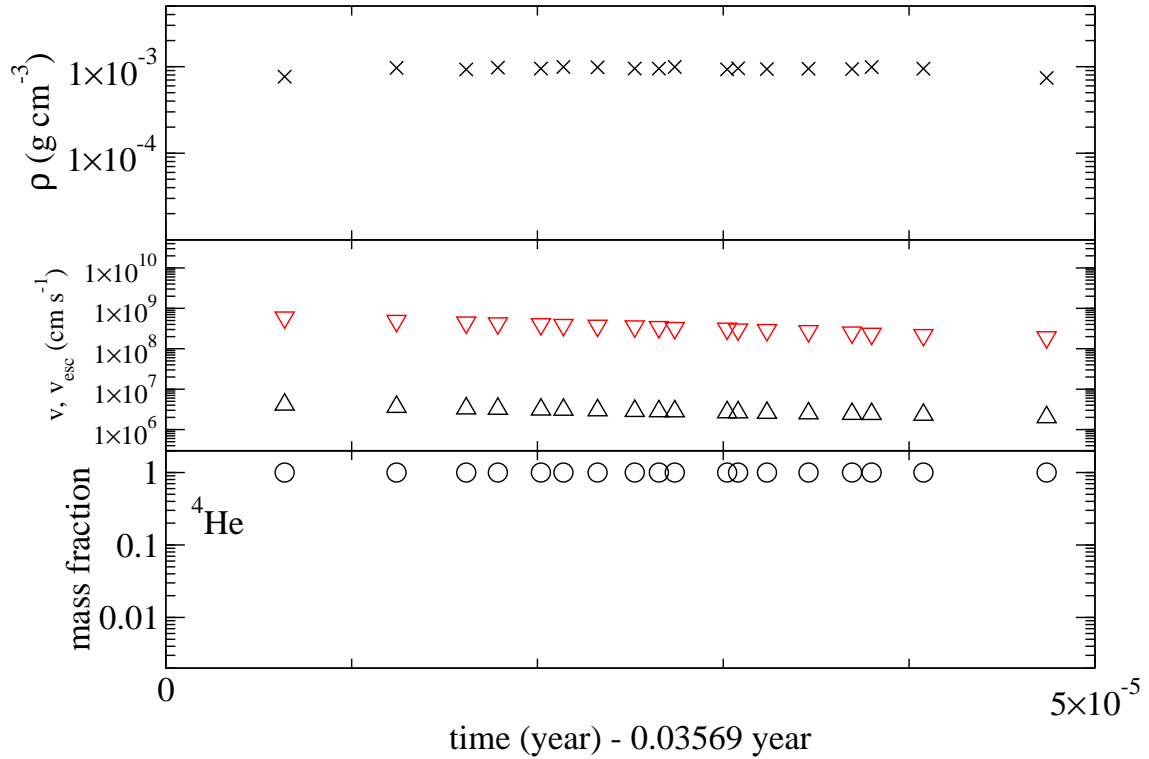


Figure 25. (*cont'd*) The mass ejection history of Model He60A including the density (top panel), velocity (middle panel) and chemical composition (bottom panel).

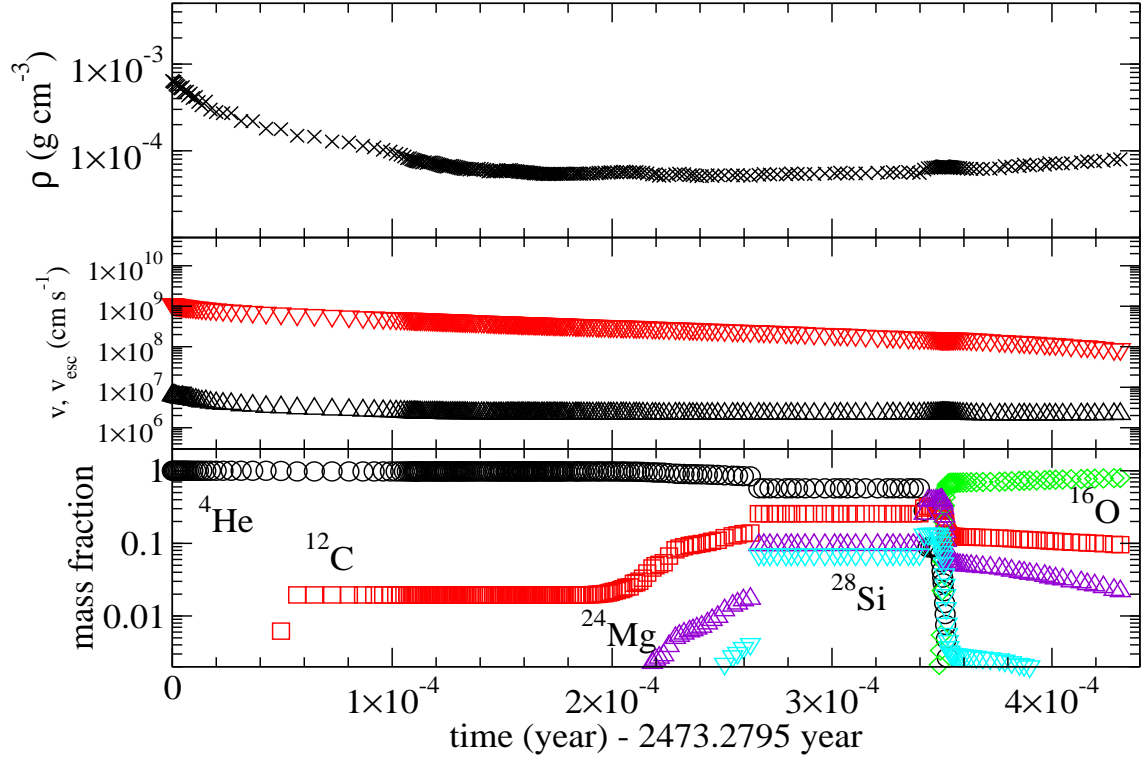


Figure 26. (*cont'd*) The mass loss history of the second strong pulse in Model He62A.

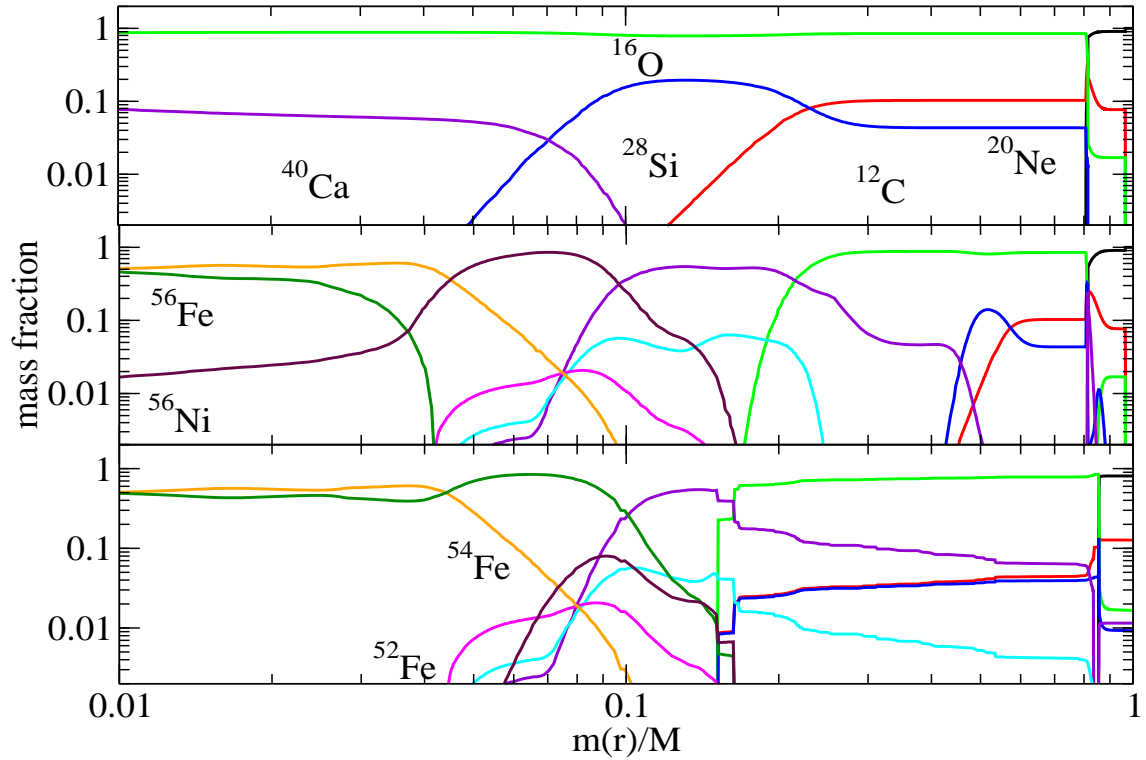


Figure 27. The chemical composition of Model He40A before the first pulse, after the first pulse and before the final pulse in the upper middle and lower plot. Here we define the star entering the pulsation phase when the core reaches $10^{9.3}$ K.

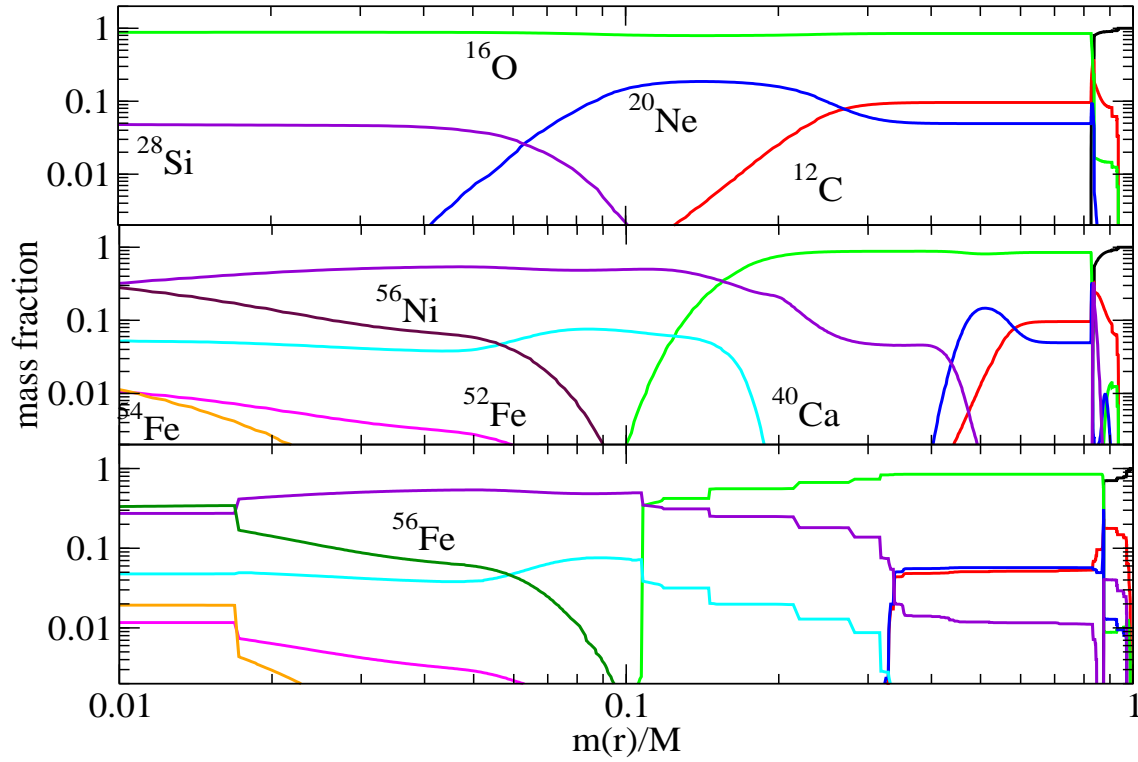


Figure 28. (*cont'd*) Similar to Figure 27, but for Model He50A before the first pulse, after the first pulse and before the final pulse in the upper middle and lower plot.

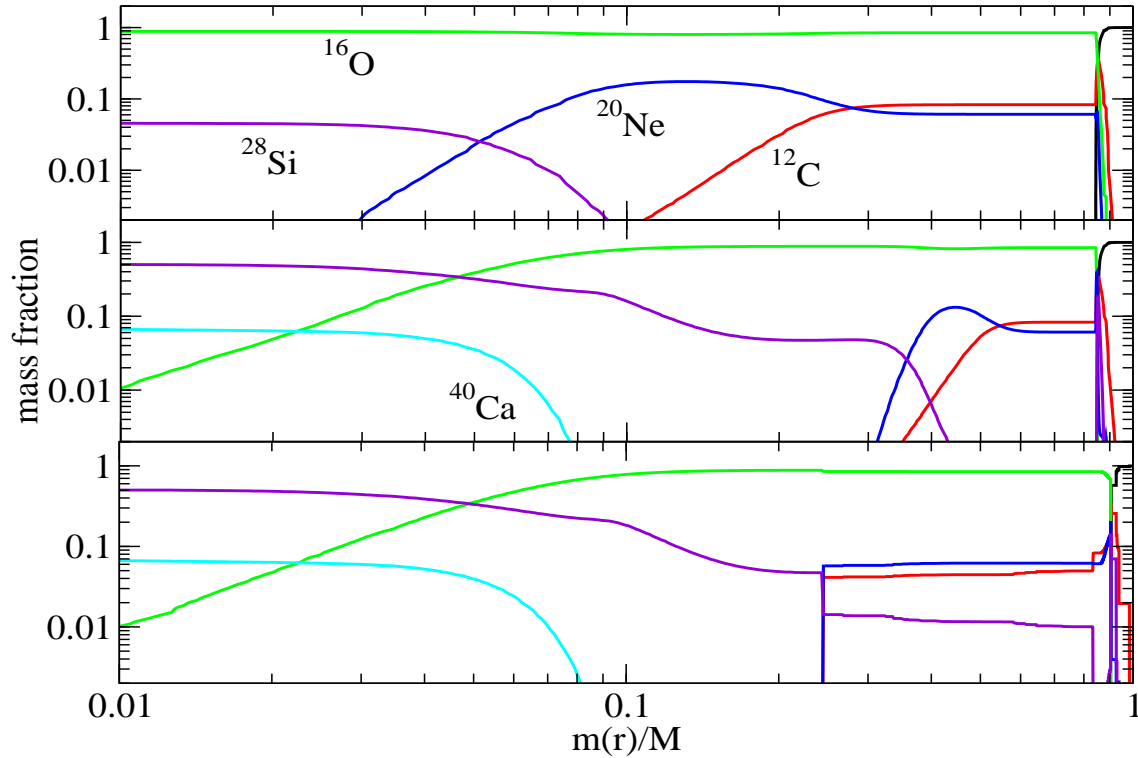


Figure 29. (*cont'd*) The abundance patterns for Model He62A before the first pulse, after the first pulse and before the second pulse.

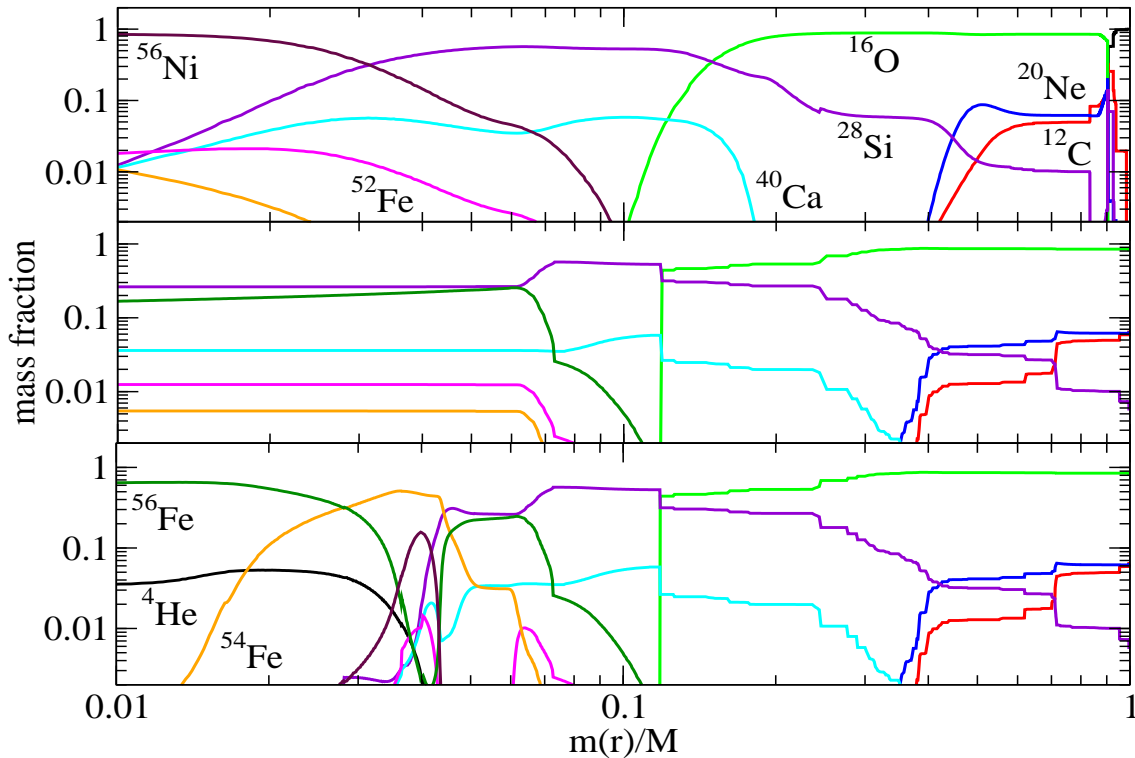


Figure 30. (*cont'd*) (Similar to Figure 29, but for Model He62A after the second pulse, before the final pulse and at the end of simulation.

can create distinctive isotope abundances in the star. By comparing the isotope distribution, we can understand which part of burning contributes to the evolution of pulsation.

In all models, it can be seen that the star is simply a pure O-core with a minute amount of Si in the core or C in the envelope, covered by a pure He surface. However, their changes can be very different depending on the progenitor mass.

In Model He40A, after the strong pulse, due to its previous weak pulses which continue to burn matter in the core, a range of elements are produced including ^{52}Fe , ^{54}Fe , ^{56}Fe and also ^{56}Ni . There is a clear structure for each layer, which comes in the order of ^{56}Fe , ^{54}Fe , ^{56}Ni , ^{40}Ca , ^{16}O and then ^4He . After that, the core relaxes and becomes quiescent until it completely loses its thermal energy produced during the pulse, while at the same time convection re-distributes the matter for a flat composition profile. Most convection occurs at $q > 0.1$, where the convective shells of different sizes make a staircase like structure.

Models He45A and He50A share a similar nuclear reaction pattern. We choose Model He50A as an example. The strong pulse provides the required temperature and density to make Ni in the center and Si in the outer zone. The Si-rich zone extends to $q \approx 0.2$. During the quiescent phase, convection not only mixes the material

in the envelope, but also in the core, which is seen by the stepwise distribution of ^{52}Fe and ^{54}Fe .

In Models He55A, He60A and He62A share also similar abundance pattern. We choose the evolution of He62A as an example. The first pulse makes the original O-core into mostly Si and some Ca. Again, the convective mixing during the quiescent state redistributes the matter near the surface ($q > 0.25$). In the second strong pulse, the nuclear reaction is very similar to the late pulses of Model He40A and He45A. Ni forms in the innermost part, with a small amount of Fe isotopes like ^{52}Fe and ^{54}Fe . Then Si and Ca form the middle layer and at last the He envelope appears. During the quiescent phase, the convection occurs in a deeper layer compared which is absent in lower mass models.

5. MODELS FOR SUPER-LUMINOUS SUPERNOVAE

PPISNe have been used to model the superluminous supernovae such as SN2006gy (Woosley et al. 2007), SN2010gx, PTF09cnd (Sorokina et al. 2016) and PTF12dam (Tolstov et al. 2017). PTF09cnd and PTF12dam are challenging as they require such massive CSM as 20 – 40 M_{\odot} CSM prior to the supernova explosions. Furthermore, these SLSNe are of Type I so that CSM needs to be H-free with the presence of He, C and O in order to explain the high opacity surrounding.

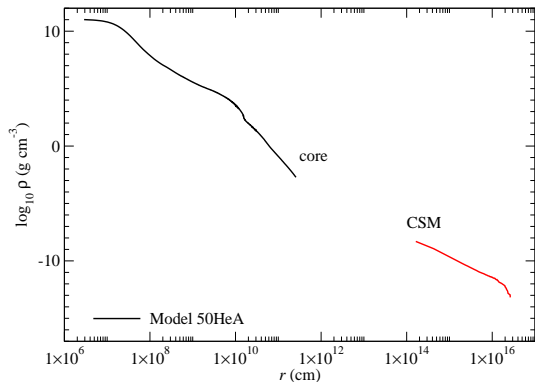


Figure 31. The final density profile for Model He50A including the core and ejecta matter (CSM) at the onset of collapse.

Models with $\sim 64 M_{\odot}$ He core is likely to eject a mass $\sim 22 M_{\odot}$. Our model gives an ejecta with He, C and O masses of 8.5, 1.8, 9.9 M_{\odot} . The corresponding ratio of He:C is therefore 4.8:1:5.5. This is close to the values in the model M66R170E27(CSM19) of Tolstov et al. (2017), which has an abundance of C:O = 1:4. Whether the following collapse of this $\sim 40 M_{\odot}$ remnant can explode energetically with an energy of $2 - 3 \times 10^{52}$ erg is uncertain.

In Figure 31 we plot the density profile of Model He50A at the onset of collapse ($\rho_c = 10^{10} \text{ g cm}^{-3}$). Both the CSM and core are included. The CSM is constructed from the mass ejection history, which is obtained by a post-process manner until the core begins to collapse. The core consists of a compact Fe core of $\sim 2 M_{\odot}$ with $r < 10^8$ cm. Outside the Fe core, a smooth Si-rich envelope extends up to $M(r) \sim 10 M_{\odot}$ and $r \sim 10^{10}$ cm. The outer surface extends to $\sim 10^{12}$ cm. We remark that the outermost envelope is mostly the remaining matter which is not ejected near the end of pulsation event. They are mostly decoupled gravitationally from the core. The original stellar envelope is the middle envelope of the final density profile.

As discussed in Section 4.8, the mass ejection of He50A is smooth which occurs for 0.0002 year (~ 2 hours) before the outermost shell is bounded. Such continuous mass ejection can produce a smooth and extended CSM outside the star. There is no significant collision among ejected masses, where the collision can give rise to observable density discontinuities. Without mass collision, the CSM profile in general follows the $1/r^2$ scaling, which extends from 10^{14} to 10^{16} cm. We note that in the calculation, there is a gap between the outer envelope of the core to the inner boundary of the CSM from 10^{11} to 10^{14} cm. There should be fallback by gravitational tidal force on the ejecta. However, to

Table 5. The primary and secondary black hole masses with one or both black hole masses exceeding $30 M_{\odot}$ within one sigma. Events in bold font are those with black hole masses exceeding $40 M_{\odot}$. m_1 and m_2 are the black hole masses in units of M_{\odot} . The data are taken from The LIGO Scientific Collaboration et al. (2018).

Event	m_1	m_2
GW150914	$35.6 \pm_{3.0}^{4.8}$	$30.6 \pm_{4.4}^{3.0}$
GW151012	$23.3 \pm_{5.5}^{14.0}$	$13.6 \pm_{4.8}^{4.1}$
GW170104	$31.0 \pm_{5.6}^{7.2}$	$20.1 \pm_{4.5}^{4.9}$
GW170729	$50.6 \pm_{10.2}^{16.6}$	$34.3 \pm_{10.1}^{9.1}$
GW170809	$35.2 \pm_{6.0}^{8.3}$	$23.8 \pm_{5.1}^{5.2}$
GW170814	$30.7 \pm_{3.0}^{5.7}$	$25.3 \pm_{4.1}^{2.9}$
GW170818	$35.5 \pm_{4.7}^{7.5}$	$26.8 \pm_{5.2}^{4.3}$
GW170823	$39.6 \pm_{6.6}^{10.0}$	$29.4 \pm_{7.1}^{6.3}$

resolve this one requires another hydrodynamical experiment to follow how the ejecta exchanges momentum.

6. BLACK HOLE MASSES FROM PULSATONAL PAIR-INSTABILITY SUPERNOVAE

The gravitational wave detectors aLIGO and VIRGO have recently detected gravitational wave signals from merger events of compact objects. Some massive black holes, for example in GW 150914, the black hole masses of $35.6 \pm_{3.0}^{4.6}$ and $30.6 \pm_{4.4}^{3.0} M_{\odot}$ are measured (Abbott et al. 2016b). Another massive black hole merger event is GW 170104, where the binary consists of black holes of masses 31.0 and 20.1 M_{\odot} respectively. In Table 6 we list out the recent gravitational wave events with black hole masses reaching above $30 M_{\odot}$ within one sigma. A recent statistics has further pushed the maximum pre-merger black hole mass to $\sim 55 M_{\odot}$ (The LIGO Scientific Collaboration et al. 2018). It is unclear, whether the massive black hole forms directly from the collapse of a massive star, or has experienced multiple merger events prior to the event detected by the gravitational wave detectors.

Our model suggests that the single star scenario has an upper limit for the black hole mass. He core with a mass greater than $64 M_{\odot}$, the star does not collapse, but explode as a pair-instability supernova. The collapse only reappears for a star with a mass larger than $260 M_{\odot}$ (for zero metallicity) (Heger & Woosley 2002). The corresponding black hole mass is $\sim 100 M_{\odot}$.

To connect PPISN with the measured black hole mass spectra, we plot in Fig. 32 the remnant mass against progenitor mass, and the mass range of the black hole measured by the gravitational wave signals. He cores with a mass between $40 - 64 M_{\odot}$, a mass correction is included to account for the pulsation-induced mass

loss. Beyond $M_{\text{He}} = 64 M_{\odot}$ the star enters the pair-instability regime and no compact remnant object is left. Near $\sim 62 M_{\odot}$ the remnant mass is the maximum at $\sim 52 M_{\odot}$. Some of the events can be explained by the current PPISN picture. This includes the primary black hole in the events GW150914, GW170104, GW170729, GW170809, GW170818 and GW170823 and the secondary black hole in the event GW170729.

We remark that there exists high uncertainties in how to connect the He core mass with the final remnant mass. In our simulations, the pulsation induced mass loss is done in one-dimension. When the multi-dimensional effects, e.g. Rayleigh-Taylor instabilities, can be considered during the propagation of pulse, the actual mass loss can be changed. Also, after the Fe core collapses, during formation of proto-neutron star and black hole, the mass ejection and neutrino energy may reduce the final remnant mass by $\sim 10\%$ (See e.g. Zhang et al. (2008); Chan et al. (2018)). We remark that interpreting the He core mass as the final remnant mass can only be an upper limit of the black hole mass. The black hole accretion disk around a rotating black hole allows formation of high velocity jet. The magnetohydrodynamical instability of the accretion disk can easily fragment the disk and send the energetic jet to the stellar envelope. This process can lower the remnant mass. Therefore, as a first estimation of our result, we use the He core mass as an upper estimate of the final black hole mass.

We note that in a single observation, the solution for matching the black hole mass with our remnant mass is degenerate for both mass and metallicity. To further apply the black hole information in PPISN to constrain the mass loss, population of black hole mass will become important, which can directly constrain the current mass loss model, when combined with suitable stellar initial mass functions.

In Figure 33 we plot the final stellar mass, C- and O-core masses for all the He-core models. We define the boundary of the C- and O-cores to be the inner boundaries where the local ${}^4\text{He}$ and ${}^{12}\text{C}$ mass fractions drop below 10^{-2} . We can see that three layers appear. For $M_{\text{He}} = 40, 45$ and $50 M_{\odot}$, there are explicit He-envelope, C- and O-layers. For $M_{\text{He}} = 55$ and $60 M_{\odot}$, the huge mass loss completely ejects the pure He layer, which exposes the C-rich layer (combined with He). At $M_{\text{He}} = 63 M_{\odot}$, the mass ejection further shreds off the C-rich layer, exposing the O-layer. The whole star has everywhere the mass fraction of ${}^{12}\text{C}$ below 10^{-2} . Therefore, the He-core and C-core masses coincide with the stellar total mass. From this we can see to what level the mass ejection takes place for the PPISN models. However, the definition of He- and C-core masses can be ambiguous at the

end of simulations because the matter becomes O-rich before C is exhausted. Similarly on the surface there can be non-zero abundance of ${}^{12}\text{C}$ instead of pure ${}^4\text{He}$.

7. CONCLUSIONS

In this paper, we studied pulsational pair-instability (PPI) which occur in the He-core of $M_{\text{He}} = 40 - 64 M_{\odot}$. These are the cores of $80 - 140 M_{\odot}$ main-sequence stars. We used the one-dimensional stellar evolution code MESA and applied the implicit hydrodynamics module implemented in the version 8118.

- (1) First, we computed the evolution of stars with the initial masses of $80 - 140 M_{\odot}$ and metallicities of $Z = 0.01 - 1 Z_{\odot}$ from the pre-main-sequence until the central temperature reaches $10^{9.3}$ K. We examined how the final He- and CO-core mass depends on the metallicity. The star with a higher metallicity has a stronger stellar wind mass loss, thus forming a smaller mass He-core. In order for the star to form a He-core of more massive than $40 M_{\odot}$ and thus to undergo PPI, $Z \lesssim 0.5 Z_{\odot}$ is required.
- (2) We calculated the evolution of the He-cores of $M_{\text{He}} = 40 - 64 M_{\odot}$ with $Z = 0$ from the He main-sequence through the onset of collapse. These He cores undergo PPI. We calculated the hydrodynamical evolution of PPI with mass ejection. We examined nucleosynthesis during PPI, showing how each pulsation changes the chemical composition of the star and how the later convection alters the post-pulsation star.
- (3) The total ejected mass is almost a monotonically increasing function of M_{He} except for some fluctuations in the lower mass end. The He-core with a higher mass has fewer weak pulses that do not eject masses. Instead it has much stronger pulses eject masses. The number of pulses ranges from 6 weak pulses for $M_{\text{He}} = 40 M_{\odot}$ to no weak pulse but 2 strong pulses for $M_{\text{He}} = 62 M_{\odot}$. The ejecta mass is lower than $1 M_{\odot}$ in the low mass end and increases to as large as $\sim 10 M_{\odot}$ near the pair-instability supernova regime. Models with $M_{\text{He}} > 64 M_{\odot}$ behave as pair-instability supernovae, where no remnant is left.
- (4) The ejecta form circumstellar matter (CSM). The composition and kinematics of the ejecta are sensitive to M_{He} . The lower mass He-cores with $M_{\text{He}} \lesssim 55 M_{\odot}$ eject only the He-envelope. More massive cores eject a part of the CO layer. The most massive core studied of $M_{\text{He}} = 62 M_{\odot}$ ejects even the Si-layer. Such heavy elements may largely alter the opacity of the CSM.
- (5) We examined the connections of PPISN, especially the ones with massive mass ejection, with the recently observed Type I super-luminous supernova (SLSN-I) PTF12dam. We show that the PPISN model produces massive enough CSM, which may be able to explain some super-luminous supernovae (includ-

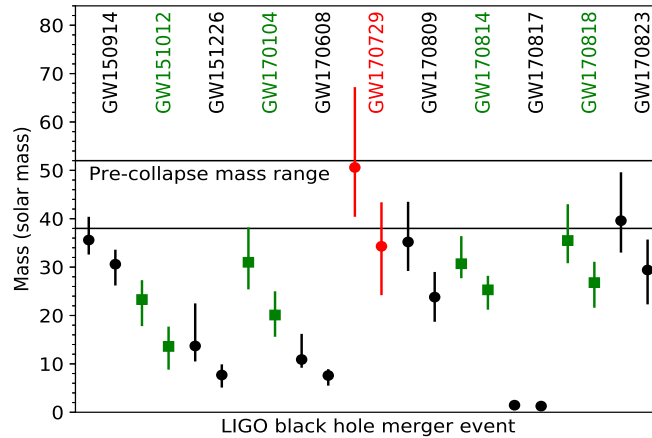


Figure 32. The pre-collapse mass of the PPISN against progenitor mass with the measured black hole masses obtained from binary black hole merger events (Abbott et al. 2016a,b, 2017; The LIGO Scientific Collaboration et al. 2018). The left and right data points correspond to the primary and secondary black holes respectively. The error bars for the pre-merge neutron star for GW170817 are too small to be seen in the current scale.

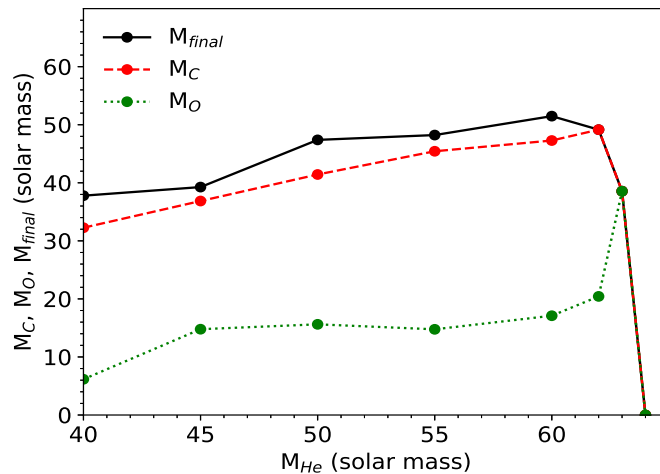


Figure 33. The pre-collapse mass of the PPISN, C- and O- core mass against progenitor He-core mass. Here we define the C- and O-cores to be the inner boundaries where the local ${}^4\text{He}$ and ${}^{12}\text{C}$ mass fractions drop below 10^{-2} .

ing PTF12dam), based on the CSM interaction. The amount of C and O is consistent with the light curve models of SLSNe-I.

(6) We compare the masses of black holes detected from the gravitational wave (GW) signals with the black hole masses after the mass ejection of PPISNe. Our PPI models predict that the expected black hole masses are $\sim 38 - 52 M_{\odot}$, i.e., the upper limit of the black hole mass is $52 M_{\odot}$. This is consistent with the current observations. Some of the events, especially GW 170729 which shows a progenitor mass of $\sim 50 M_{\odot}$, could be a remnant left behind by PPISN. The upper limit of

the black hole mass can form the lower mass limit of the mass gap of the massive black holes (i.e. the transition from black hole to no-remnant). Future observations of the black hole mass spectrum derived from the merger events of binary black holes can provide the corresponding constraints on such mass limit. The detection of black hole mass prior to the merger event between ~ 50 and $\sim 150 M_{\odot}$ can challenge the current black hole formation mechanism and its progenitor evolution, and provide insight to the implied merging event rate of massive black holes evolved from PPISNe.

(7) In the future work, we will focus on the observables of the PPISN in terms of neutrinos and light curves. Using our hydrodynamics model, the expected neutrino signals detected by terrestrial and the expected light curve will be calculated. The results will provide a more fundamental understanding to the properties of PPISN, which may be constrained from the observables of one the the PPISN candidates.

(8) In the appendix we show that our results are qualitatively consistent with the results in the literature, although some minor differences can be found.

8. ACKNOWLEDGMENT

This work has been supported by the World Premier International Research Center Initiative (WPI Initiative), MEXT, Japan, and JSPS KAKENHI Grant Number JP17K05382. S.B. work on PPISN is supported by the Russian Science Foundation Grant 19-12-00229. We thank the developers of the stellar evolution code MESA for making the code open-source. We also thank Raphael Hirschi for the insightful discussion in the stellar evolution of PPISN and his critical comments. We at last thank Ming-Chung Chu for his assistance in editing the manuscript.

Software: MESA (v8118; (Paxton et al. 2011, 2013, 2015, 2017))

APPENDIX

A. COMPARISON WITH MODELS IN THE LITERATURE

A.1. *Yoshida et al. (2016)*

In this section we compare our results with some representative PPISN models in the literature.

In *Yoshida et al. (2016)*, the PPISN model of mass from about $54 M_{\odot}$ to $60 M_{\odot}$ (corresponding to a progenitor mass from $140 M_{\odot}$ to $250 M_{\odot}$ in zero metallicity) are computed. In that work, the calculation is separated into two parts. During the quiescent and pre-pulsation phases, the hydrostatic stellar evolution code is used. During the pulsation phase, the star model is transferred to the dynamical code PPM, which follows the expansion of the star until the mass ejection has ended ($\sim 10^4$ s). Then they map the results to the stellar evolution code again until the next pulsation.

Their $140 M_{\odot}$ and $250 M_{\odot}$ models have similar configurations as our Models He55A and He60A. First, in their $140 M_{\odot}$ model ($250 M_{\odot}$ model), they observe a total of six (three) pulses which ejected 3.99 (7.87) M_{\odot} of matter before collapse. Model He55A (He60A) exhibits three (two) pulses before collapse, which ejects 6.78 (8.52) M_{\odot} of matter. Our models show a smaller number of pulses, but give similar ejecta mass. This means our models can capture the energetic pulse well, but not the smaller pulses.

Then we compare the ejection timescales. The $140 M_{\odot}$ ($250 M_{\odot}$) model show all pulses within a period of 0.92 (1434) years, while Model He55A (He60A) shows all pulses within a period of 1341 (2806) years. There is a huge difference in the pulsation period in our Model He55A and their $140 M_{\odot}$ model. We notice that the difference comes from the strengths of the pulses. In particular, our second pulse leads to a transition about 100 years while ejecting $1.45 M_{\odot}$. The most similar event in their model is the fourth pulse, but with a transition of only 0.279 year.

At last we compare the final core composition. The $140 M_{\odot}$ ($250 M_{\odot}$) model has an Fe (CO) core mass at 2.57 (43.51) M_{\odot} , while in our model, we have 2.49 (38.60) M_{\odot} for the Fe (CO) mass. This shows that, despite the difference in the mass ejection history, our models can still capture the major mass ejection events, which results in a similar mass ejection and core composition. However, there is a strong pulse in our He55A model, which is not seen in their $140 M_{\odot}$ model.

A.2. *Woosley (2017, 2019)*

Next, we compare our models with the models from *Woosley (2017)*. We have chosen the PPISN close to that work; in particular, ours Models He40A, He50A, He60A and He62A can be compared directly with the He40, He50, He60 and He62 models. In *Woosley (2017)*, the Kepler code, which consists of both hydrostatic and hydrodynamics components, is used to follow the whole evolution of PPISN.

First we compare the mass ejection history. In *Woosley (2017)*, there are 9, 6, 3 and 7 pulses with a total mass loss of 0.97, 6.31, 12.02 and 27.82 M_{\odot} for Models He40, He50, He60 and He62 respectively. In our models, we have 6, 3, 2 and 2 pulses with a total mass loss of 2.22, 2.61, 9.52 and 12.85 M_{\odot} for Models He40A, He50A, He60A and He62A respectively. Again, our code tends to produce fewer pulses and the pulses in general eject fewer matter. One of the differences is how shock is treated. For a shock-capturing scheme with a larger dissipation, the kinetic energy will be partly dissipated into thermal energy, such that the star is globally thermalized instead of ejecting matter through kinetic pulses. Another origin of the differences can be related to the nature of the instability of PPISN. Since the

trigger of the explosive O-burning comes from the pair-instability, which is very sensitive to the initial condition (e.g. how we evolve the stellar evolution model before the pulsation and between pulses) and numerical treatment (e.g. how convection and mass ejection are treated). For example, a stronger contraction can lead to more O-burning in the core, which gives much stronger pulsation and hence more mass loss. In fact, such dependence can also be seen in other field. For example, in the propagation of flame, since it is unstable towards hydrodynamics instability, (Glazyrin et al. 2013). The burning history can be highly irregular in the unstable regime.

Next we compare the timescale of the pulsation. In this work, the whole pulsation until collapse last for 0.38, 61.3, 2806 and 6610 years for the four models, while in Woosley (2017) they are 2.48×10^{-3} , 0.38, 2695 and 6976 years. It shows that for massive He cores, our results agree with their work but there are large differences when the He core becomes less massive. In that case, our final pulse is always strong enough to re-expand the star again before the final collapse, which significantly lengthens the pulsation period.

Then we compare the Fe core mass. In Woosley (2017) the core has 2.92, 2.76, 1.85 and $3.19 M_{\odot}$ Fe. In our models, we have 3.42, 1.73, 1.64 and $2.66 M_{\odot}$. There is a dropping trend from Model He40A to He60A, which corresponds to the trend that the pair-instability occurs at a lower density when the mass increases. On the other hand, near the pair-instability regime, the pulsation becomes sufficiently vigorous which enhances the NSE-burning.

At last we compare the explosion energy. We compare the Model He62A, which has the largest explosion energy. In our model, in the second big pulse, the star has its total energy increased by 2.0×10^{51} erg while the maximum kinetic energy achieved is 2.8×10^{51} erg. This is very similar to the result in Woosley (2017), where the pulse is observed to have a kinetic energy of 2.8×10^{51} erg.

One major difference we notice is in the pair-instability limit, for Model He64A, our model shows a higher explosion energy. Across the strongest pulse, there is a change of total energy by 1.6×10^{52} erg, where the maximum kinetic energy of the system is $\sim 1.7 \times 10^{52}$ erg. In Woosley (2017) the kinetic energy is reported to be 4×10^{51} erg. We observe that the difference comes from the number of pulsation, where our Model He64A has two big pulses but only one in their work. The first pulse has incinerated the ^{16}O in the core while ejecting on the surface. This means that the star has to reach a more compact state before the star can explode. As a result, the amount of energy produced in the exploding pulse is much larger.

Our results show a systematically lower number of pulses with slightly lower ejecta mass. The pulsation periods qualitatively agree with each other except for models with a final strong pulse, which may significantly lengthen our pulsation period. Also, in our explosion models, the system tends to store the energy in terms of internal energy instead of kinetic energy, as a result, the star tends to expand globally, where the excess energy and momentum of the star is transferred mostly to the surface. This ejects the low density matter and leaves a bounded and hot massive remnant. Despite the differences in the pulsation, globally the nucleosynthesis agrees with each other because most of the heavy elements are produced by the strong pulses, where our results are consistent with those in the literature.

In Woosley (2019), the He star models are further evolved with mass loss. The solar metallicity of the Fe group is assumed in the mass loss rate for He stars. We note that this is not consistent with the mass loss history from the main-sequence, because the He core of the solar metallicity star becomes too small to undergo PPI (see our Figure 8). The final black hole mass is lower compared to his previous work. We notice that the PPISN models in this work have in general stronger pulsations. A 50 (60) M_{\odot} He-core ejects $\sim 7(57) M_{\odot}$, which is much higher than $\sim 6(12) M_{\odot}$ mass ejection in his previous work. Our results are closer to his previous work. This might depend on the thickness of the He layer which is determined by the mass loss history.

A.3. Marchant et al. (2018)

This work is one of the recent work which uses the same MESA code (Version 11123) (Paxton et al. 2017) to evolve the evolutionary path of PPISN. Their work has a similar setting to this work. Here we briefly compare their results with our results.

They have computed an array of single star models from 40 – 240 M_{\odot} with semi-convection, Riemann solver using the HLLC solver and the *approx21* nuclear reaction network. They treat the mass loss of the star by considering the average escape velocity.

Our work agrees qualitatively with theirs. For a lower mass He core model, some distinctive differences can be seen. For example, in their models, multiple pulsations are observed. They observe a total of 4 pulses for the 54 M_{\odot} stars (corresponds to 39.73 M_{\odot} at He depletion). On the other hand, our 40 M_{\odot} He star model gives a total of 6 pulses. They observe in total 0.63 M_{\odot} mass ejection before collapse while ours is about 2.2 M_{\odot} . The duration in their model

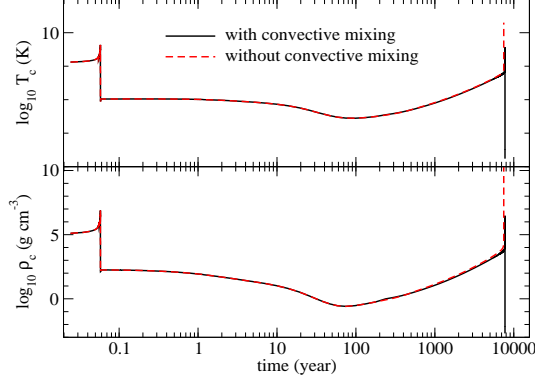


Figure 34. (upper panel) The central temperature against time for Model He60A with and without convection. (lower panel) Similar to the upper panel, but for the central densities.

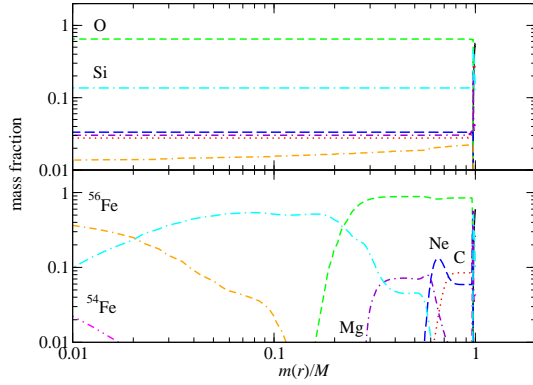


Figure 35. The chemical abundance profiles for Model He60A prior to its second contraction at a central temperature $\approx 10^9$ K with convection (upper panel) and without convection (lower panel).

is shorter ($\sim 7 \times 10^{-4}$ year) but ours is longer (~ 0.02 year) after the onset of pulsation. For a higher mass He core model such as $\sim 87 M_{\odot}$ (corresponds to $60.04 M_{\odot}$ at He depletion). They show only 2 pulses, which is the same as our $60 M_{\odot}$ He star model. The duration also agrees with each other (their model shows a duration of 7.5×10^3 years while ours is shorter at 3×10^3 years. A total of $4.6 M_{\odot}$ mass loss is found in their model (the pre-He depletion mass loss is excluded) while ours is at a higher value $\sim 8.5 M_{\odot}$.

We notice that their models and our models do not completely agree with each other. We notice that there are some critical differences in the implementation of this work from their work. First, they consider the evolution of the H-free stars, with a metallicity at $0.1 Z_{\odot}$. The He-core mass is therefore a function of the progenitor mass, instead of a direct model parameter as controlled in our models. Furthermore, they use the Riemann solver (HLLC) in the newer version instead of the artificial viscosity scheme. How the pulse transfers into shock at the near-surface area can be different.

B. EFFECTS OF HYDROSTATIC CONVECTIVE MIXING

In Woosley (2017) the PPISN is prepared for models with convective mixing. It is mentioned that the convective mixing is essential to evolve the star correctly to readjust the chemical composition of the remnant. It is unclear how much the convective mixing can change the evolutionary path of the PPISN. Here we compare the model of He60A by treating the convective mixing as an adjustable parameter. In Figure 34 we plot the central temperature (upper panel) and central density (lower panel) against time for Model He60A for both choices. It can be seen that the effects of convective mixing are huge. In the model with mixing switched on, in the second pulse it leads to a large amplitude expansion, which leads to significant mass loss afterwards before its third contraction to its collapse. On the other hand, the model without convective mixing has a faster growth of central temperature and central density, where the star collapses without any pulsation.

To understand the difference, we plot in Figure 35 the chemical composition of the star before the second contraction takes place. We pick both star models when it has a central temperature of 10^9 K. It can be seen that the role of

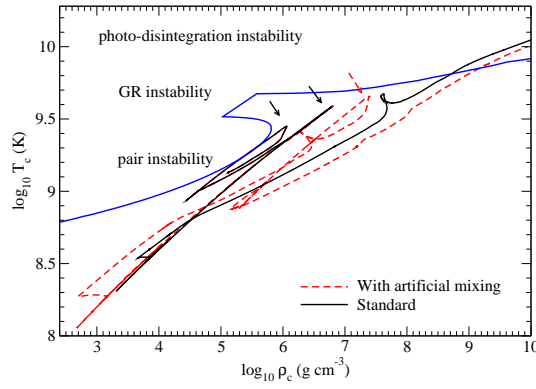


Figure 36. The central temperature against central density in \log_{10} scale for two models, the He60A with standard mixing scheme (See also Section 2) and with artificial enforced mixing scheme. The blue lines and the arrows follow the same meaning as in Figure 14. The arrows (black solid arrows and red dashed arrow) are the moments of the pulsation for the tested models.

convective mixing is clear that the mixing not only re-distribute the energy of the matter, the composition in the large-scale is modified. A considerable amount of fuel is re-inserted into the core, which contains O and Si from the unburnt envelope, and some remained ^{54}Fe and ^{56}Fe produced in the first contraction. This shows that the convection during the expansion is important for the future nuclear burning to correctly predict the strength of the pulse, which affects the nucleosynthesis as well as the mass loss.

To further demonstrate the importance of convective mixing to the strength and number of pulsations, we perform some contrasting study of two models, one is Model He60A the other is similar to He60A, but with enhanced mixing. We have shown in Section 4 from the Kipperhahn diagram that the convection mixing in Model He60A is less strong that during its quiescent phase after pulsation, the star does not exhibit the global convective phase, unlike other models like He40A, He50A and He62A. So, this model becomes a good candidate to demonstrate the effects of convective mixing between pulsation. To provide the enhanced mixing, we enforce the whole star to undergo mixing process during its expansion and when it is fully relaxed. We defined the critical temperature be 10^9 K below that the star is fully relaxed for convective mixing.

In Figure 36 we plot the central temperature against central density (both in logarithmic scale) for the two models. The evolution of He60A is exactly the same as that presented in previous section. Here, we look into more details for the model with artificial mixing. Before the second pulse, the two models exhibit exact the same trajectories. It is because the central temperature has barely reached below 10^9 to trigger the mixing. But after the second pulse, which has mass ejection, its central temperature goes below 10^9 K. The one with enhanced mixing, because it involves mixing material with the outer elements, which has in general lower temperature and lower atomic mass, it can reach a low central temperature during its expansion. Also, the mixing process brings in the C- and O-rich material into the core. In the third contraction, unlike the "standard" model presented in the main text, the core exhibits the third pulsation. However, the strength is not strong enough to trigger mass loss on the surface. Then, although the core reaches one more time below the 10^9 for the hand-made convective mixing, the O-abundance of the star becomes too low that the core becomes massive enough to collapse directly, without triggering the fourth pulsation.

C. EFFECTS OF ARTIFICIAL VISCOSITY

Another important parameter in numerical hydrodynamics modeling is the artificial viscosity. Owing to the lack of Riemann solver (exact or approximate) for the spatial derivative, artificial increases of pressure is needed to prevent the shock from over-clumping the mass shells. However, the artificial viscosity formula contains one free parameters C_{av} . The default value from the package 'ccsn' in the

Software: MESA test suite is $C_{av} = 2 \times 10^{-2}$. To probe the effects of this parameter, we carry out a control test by varying C_{av} .

In Figure 37 the time dependence of the central temperature (upper panel) and central density (lower panel) are plotted for Model He60A with $C_{av} = 2 \times 10^{-3}$, 2×10^{-2} (default value) and 2×10^{-1} . Results with $C_{av} = 2 \times 10^{-3}$ and 2×10^{-2} are almost identical. This shows that the default choice of C_{av} can maintain the shock propagation and produce convergent results. On the other hand, when $C_{av} = 2 \times 10^{-1}$, very different outcome appears. The first

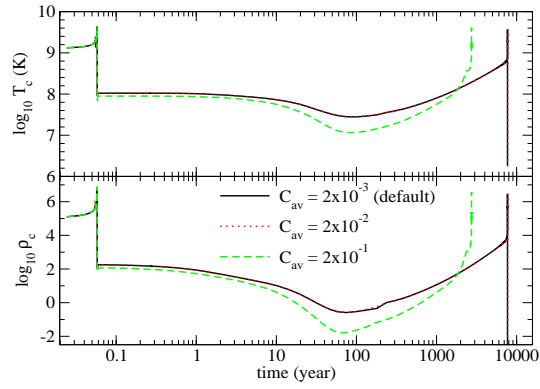


Figure 37. (upper panel) The central temperature against time for Model He60A with different levels of artificial viscosity. (lower panel) Similar to the upper panel, but for the central densities.

expansion has reached to a lower central temperature and density. Furthermore, the two quantities are in general lower than the cases with lower C_{av} during the expansion. The second contraction also takes place a few thousand years before the other two cases. This shows that if a too large artificial viscosity is chosen, the pressure heating also alters the shock heating and its associated nuclear burning in the star, thus affecting the consequent configurations.

D. EFFECTS OF HYDRODYNAMICS CONVECTIVE MIXING

In the main text we have mentioned that the role of convective mixing is less important in the hydrodynamics during shock outbreak because the typical timescale of convective mixing is longer than the hydrodynamical timescale. However, it remains interesting to examine when convective mixing is included, how it changes the evolutionary path. In fact, a more consistent and accurate approach to follow the evolution requires the input of convective mixing, but it always induces numerical instabilities which impedes any further evolution. Here we attempt to study how convective mixing affects the pulsation history of PPISN.

In the left panel of Figure 38 we plot the speed of sound, fluid velocity and convective velocity for the Model He40A when it is rapidly contraction before the first pulse at a central temperature of $10^{9.6}$ K. We can see that, indeed, the convective velocity is about $\sim 1\%$ of the speed of sound, while the fluid velocity is less than 10^{-4} of the speed of sound. The star is close to hydrostatic equilibrium, in contrast to the massive star $\sim 60M_{\odot}$ counterpart. The more compact structure of the star also means a shorter convection timescale. So, mixing can be influencing to the pulsation process.

As mentioned switching on convection can be problematic in the hydrodynamics. To bypass this difficulties, instead of doing mixing in the hydrodynamics, we post-process at every step the abundance profile to mimic the mixing process. Similar to the standard mixing length theory procedure, we first locate the mass shells which can undergo convection. Then we calculate the convection velocity and the corresponding mixing timescale t_{mix} . After that, we compare with the timestep Δt . If $t_{mix} < \Delta t$, complete mixing is assumed; otherwise partial mixing among the cells in the convection zone is assumed. We notice that a consistent way to do the mixing process requires mixing entropy too. However, this affects the pressure which in terms affects the dynamics. In fact, it is the mixing of fuel to the actively burning site important for the trigger of pulsation. As a first approximation, we neglect this complication.

In the right panel of Figure 38 we plot the thermodynamics trajectories of Model He40A using the default prescription (no dynamical mixing) and the described mixing process. We can see that both curves are very similar qualitatively. However, minor changes can be seen by the small scale pulses in the star. Model with dynamical mixing has fewer small pulse. The moment where the large pulse takes place differs. The model without dynamical mixing occurs at a higher $T_c \sim 10^{9.8}$ K while that with dynamical mixing occurs at a lower $T_c \sim 10^{9.75}$ K. One possibility for this difference is that for small pulse, the mixing tends to lower the ^{16}O abundance available to the active burning site, which is more local. On the other hand, the mixing allows more zone to be rich in ^{16}O when the star needs to carry out a collective burning of ^{16}O . Therefore, it can occur earlier. Despite the difference it shows that the mixing process is efficient to the lower mass PPISN but the replenishment of fuel does not particularly enhance the pulsation process.

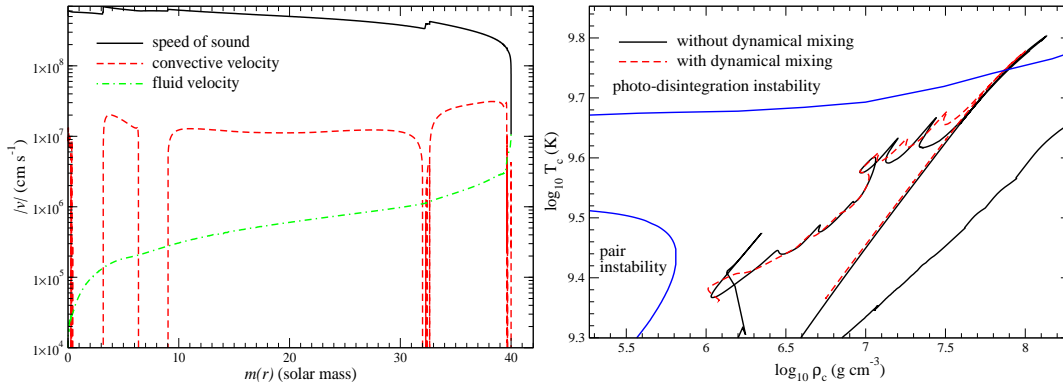


Figure 38. (left panel) The fluid velocity, speed of sound and convective velocity of Model He40A at $T_c = 10^{9.6}$ K. (right panel) The thermodynamics trajectory of Model He40A with dynamical mixing (red dashed line) and without dynamical mixing (black solid line). The blue lines and the arrows follow the same meaning as in Figure 14.

REFERENCES

- Abbott, B. P., Abbott, R., Abbott, T. D., et al. 2016a, *ApJ*, 818, L22
- . 2016b, *Phys. Rev. Lett.*, 116, 241103
- . 2017, *Phys. Rev. Lett.*, 118, 221101
- Alastuey, A., & Jancovici, B. 1978, *ApJ*, 226, 1034
- Arnett, D. 1996, *Supernovae and Nucleosynthesis: An Investigation of the History of Matter from the Big Bang to the Present* (Princeton: Princeton University Press)
- Baraffe, I., Heger, A., & Woosley, S. E. 2001, *ApJ*, 550, 890
- Barkat, Z., Rakavy, G., & Sack, N. 1967, *Phys. Rev. Lett.*, 18, 379
- Belczynski, K., Ryu, T., Perna, R., et al. 2017, *MNRAS*, 471, 4702
- Böhm-Vitense, E. 1958, *ZA*, 46, 108
- Bond, J. R., Arnett, W. D., & Carr, B. J. 1984, *ApJ*, 280, 825
- Buchler, J. R., & Yueh, W. R. 1976, *ApJ*, 210, 440
- Cassisi, S., Potekhin, A. Y., Pietrinferni, A., Catelan, M., & Salari, M. 2007, *ApJ*, 661, 1094
- Chan, C., Müller, B., Heger, A., Pakmor, R., & Springel, V. 2018, *ApJ*, 852, L19
- Chatzopoulos, E., & Wheeler, J. C. 2012, *ApJ*, 748, 42
- Chatzopoulos, E., Wheeler, J. C., & Couch, S. M. 2013, *ApJ*, 776, 129
- Chen, K.-J., Woosley, S., Heger, A., Almgren, A., & Whalen, D. J. 2014, *ApJ*, 792, 28
- Cox, J. P., & Giuli, R. T. 1968, *Principles of Stellar Structure* (New York: Gordon and Breach)
- Cybur, R. H., Amthor, A. M., Ferguson, R., et al. 2010, *ApJS*, 189, 240
- de Jager, C., Nieuwenhuijzen, H., & van der Hucht, K. A. 1988, *A&AS*, 72, 259
- Dewitt, H. E., Graboske, H. C., & Cooper, M. S. 1973, *ApJ*, 181, 439
- El Eid, M. F., Fricke, K. J., & Ober, W. W. 1983, *A&A*, 119, 54
- Ferguson, J. W., Alexander, D. R., Allard, F., et al. 2005, *ApJ*, 623, 585
- Foley, R. J., Smith, N., Ganeshalingam, M., et al. 2007, *ApJL*, 657, L105
- Fowler, W. A., & Hoyle, F. 1964, *ApJS*, 9, 210
- Fraley, G. S. 1968, *Ap&SS*, 2, 96
- Fuller, G. M., Fowler, W. A., & Newman, M. J. 1985, *ApJ*, 293, 1
- Glatzel, W., Eid, M. F. E., & Fricke, K. J. 1985, *Astron. Astrophys.*, 149, 413
- Glazyrin, S. I., Blinnikov, S. I., & Dolgov, A. 2013, *Mon. Not. R. astr. Soc.*, 433, 2840
- Glebbeek, E., Gaburov, E., de Mink, S. E., Pols, O. R., & Portegies Zwart, S. F. 2009, *A&A*, 497, 255
- Grott, M., Chernigovski, S., & Glatzel, W. 2005, *Mon. Not. R. astr. Soc.*, 360, 1532
- Heger, A., Langer, N., & Woosley, S. E. 2000, *ApJ*, 528, 368
- Heger, A., & Woosley, S. E. 2002, *ApJ*, 567, 532
- Heger, A., & Woosley, S. E. 2010, *ApJ*, 724, 341
- Hirschi, R. 2017, in *Handbook of Supernovae*, ISBN 978-3-319-21845-8. Springer International Publishing AG, 2017, ed. A. W. Alsabti & P. Murdin (Berlin: Springer), 567
- Iglesias, C. A., & Rogers, F. J. 1993, *ApJ*, 412, 752
- . 1996, *ApJ*, 464, 943
- Itoh, N., Hayashi, H., Nishikawa, A., & Kohyama, Y. 1996, *ApJS*, 102, 411
- Itoh, N., Totsuji, H., Ichimaru, S., & Dewitt, H. E. 1979, *ApJ*, 234, 1079
- Kasen, D., Woosley, S. E., & Heger, A. 2011, *ApJ*, 734, 102
- Langanke, K., & Martínez-Pinedo, G. 2000, *Nuclear Physics A*, 673, 481

- Limongi, M. 2017, in Handbook of Supernovae, ISBN 978-3-319-21845-8. Springer International Publishing AG, 2017, ed. A. W. Alsabti & P. Murdin (Berlin: Springer), 513
- Maeder, A., & Meynet, G. 2001, *A&A*, 373, 555
- Marchant, P., Renzo, M., Farmer, R., et al. 2018, *ApJ*, 882, 36
- Meynet, G., & Maeder, A. 2017, Handbook of Supernovae, ed. A. W. Alsabti & P. Murdin (Berlin: Springer), 601
- Moriya, T., Tominaga, N., Tanaka, M., Maeda, K., & Nomoto, K. 2010, *ApJL*, 717, L83
- Nomoto, K., & Hashimoto, M. 1988, *PhR*, 163, 13
- Nomoto, K., Kobayashi, C., & Tominaga, N. 2013, *ARA&A*, 51, 457
- Nugis, T., & Lamers, H. J. G. L. M. 2000, *A&A*, 360, 227
- Oda, T., Hino, M., Muto, K., Takahara, M., & Sato, K. 1994, *Atomic Data and Nuclear Data Tables*, 56, 231
- Ohkubo, T., Nomoto, K., Umeda, H., Yoshida, N., & Tsuruta, S. 2009, *ApJ*, 706, 1184
- Osaki, Y. 1966, *PASJ*, 18, 384
- Paxton, B., Bildsten, L., Dotter, A., et al. 2011, *ApJS*, 192, 3
- Paxton, B., Cantiello, M., Arras, P., et al. 2013, *ApJS*, 208, 4
- Paxton, B., Marchant, P., Schwab, J., et al. 2015, *ApJS*, 220, 15
- Paxton, B., Schwab, J., Bauer, E. V., et al. 2017, *ApJS*, 234, 34
- Pols, O. R., Tout, C. A., Eggleton, P. P., & Han, Z. 1995, *MNRAS*, 274, 964
- Potekhin, A. Y., & Chabrier, G. 2010, *Contributions to Plasma Physics*, 50, 82
- Rakavy, G., & Shaviv, G. 1967, *ApJ*, 148, 803
- Renzo, M., Ott, C. D., Shore, S. N., & de Mink, S. E. 2017, *A&A*, 603, A118
- Rogers, F. J., & Nayfonov, A. 2002, *ApJ*, 576, 1064
- Salpeter, E. E. 1954, *Australian Journal of Physics*, 7, 373
- Saumon, D., Chabrier, G., & van Horn, H. M. 1995, *ApJS*, 99, 713
- Scammapieco, E., Madau, P., Woosley, S. E., Heger, A., & Ferrara, A. 2005, *ApJ*, 633, 1031
- Smith, N. 2008, *Nature*, 455, 201
- Smith, N., Li, W., & Foley, R. D. 2007, *ApJ*, 666, 1116
- Sorokina, E., Blinnikov, S., Nomoto, K., Quimby, R., & Tolstov, A. 2016, *ApJ*, 829, 17
- Sukhbold, T., Ertl, T., Woosley, S. E., Brown, J. M., & Janka, H.-T. 2016, *ApJ*, 821, 38
- The LIGO Scientific Collaboration, the Virgo Collaboration, Abbott, B. P., et al. 2018, *Phys. Rev. X*, 9, 031040
- Timmes, F. X., & Arnett, D. 1999, *ApJS*, 125, 277
- Timmes, F. X., & Swesty, F. D. 2000, *ApJS*, 126, 501
- Tolstov, A., Nomoto, K., Blinnikov, S., et al. 2017, *ApJ*, 835, 266
- Umeda, H., & Nomoto, K. 2002, *ApJ*, 565, 385
- Vink, J. S., de Koter, A., & Lamers, H. J. G. L. M. 2001, *A&A*, 369, 574
- Woosley, S. E. 2017, *ApJ*, 836, 244
- Woosley, S. E. 2018, *ApJ*, 863, 105
- . 2019, *ApJ*, 878, 49
- Woosley, S. E., Blinnikov, S., & Heger, A. 2007, *Nature*, 450, 390
- Woosley, S. E., & Heger, A. 2015, in *Astrophysics and Space Science Library*, Vol. 412, *Very Massive Stars in the Local Universe*, ed. J. S. Vink (Switzerland: Springer International Publishing), 199
- Yoon, S.-C., Dierks, A., & Langer, N. 2012, *A&A*, 542, A113
- Yoshida, T., Okita, S., & Umeda, H. 2014, *MNRAS*, 438, 3119
- Yoshida, T., Umeda, H., Maeda, K., & Ishii, T. 2016, *Mon. Not. R. astr. Soc.*, 457, 351
- Zhang, W., Woosley, S. E., & Heger, A. 2008, *ApJ*, 679, 639